Considerations of Fusion Reactor Design and Implementations

Tristan Ruel
School of Electrical Engineering and Computer Science
University of Ottawa
Ottawa, Canada
0009-0003-3284-6174

Joshua Larocque
School of Electrical Engineering and Computer Science
University of Ottawa
Ottawa, Canada
0009-0005-9922-9394

***Abstract*— Increasing evidence for climate change has lent new urgency to the development of alternatives to fossil fuels. Magnetic fusion offers the prospect of energy production without CO_2 emission and without any possibility of accidental meltdown or long-lived actinide waste. The following manuscript will examine the considerations of nuclear fusion reactor design and implementation for nuclear engineers and the general scientific community. Looking at both the well-known advantages and the difficulties involved in developing fusion, one will explore the hurdles of harnessing fusion as a renewable energy source by examining reactor design considerations, technological limitations, implementation challenges, potential environmental consequences, and economic factors.

After a reminder of the main principles, this study aims to provide a comprehensive summary of past research conducted on nuclear fusion experiments. It seeks to analyse the advantages and drawbacks of these experiments, ultimately leading to a conclusion that highlights key sources of considerations for engineers and physicists should bear in mind as we move into the era of a new energy source, fusion.

Keywords*— *nuclear fusion, nuclear engineering, sustainable energy, tritium, deuterium, plasma physics, magnetohydrodynamics, plasma confinement, divertor physics.

I. INTRODUCTION TO FUSION REACTIONS

In order to obtain a fusion reaction, two nuclei that have a natural tendency to repel each other, both being positively charged, must be brought close together to overcome the Coulomb barrier caused by the electrostatic repulsion between two positively charged nuclei due to their mutual electromagnetic interaction. It is caused by the presence of positive protons within the nuclei, which repel each other due to their like charges. Overcoming this barrier requires providing sufficient energy to reach the zone close to the nucleus for the strong nuclear force to take effect and initiate the fusion process.

The quantification of the probability of overcoming this barrier can be achieved by measuring the "cross section" of a fusion reaction. Figure 1 illustrates the variation of the effective cross section for several fusion reactions as a function of interaction energy, specifically for light elements.

After careful observation of Figure 1 below, one is led to the emergence of several key observations to consider:

- Fusion reactions require extremely high temperatures, exceeding 100 million degrees Kelvin (10 keV), at such extreme temperatures, the atoms become ionized, the electrons are separated from the nuclei, resulting in the formation of the fourth state of matter, plasma.

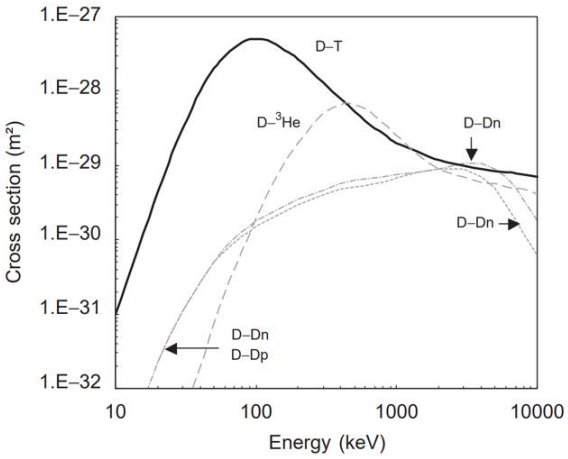

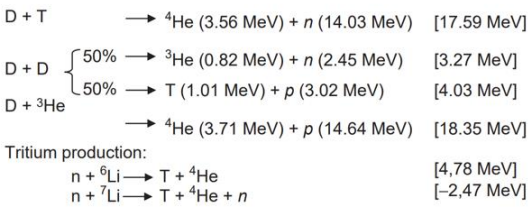

Figure 1: Cross Section of Main Fusion Reactions [1]

- The cross section of a nuclear reaction represents the effective area that particles need to collide within to undergo the desired reaction. It is measured in units of area, the barn (1 barn = 10^{-28}m^2). In the case of fusion reactions, where two atomic nuclei combine to form a heavier nucleus, the cross sections are typically on the order of 1 barn. This means that for a fusion reaction to occur, the colliding particles must come into contact within an extremely small region. In comparison to fission reactions, which have larger cross sections, where a heavy nucleus is split into two smaller nuclei. The fission of ^{235}U, for example, can be achieved with thermal or slow neutrons and has a cross section of about 600 barns. This means that fission reactions are much more likely to occur with a greater probability when compared to fusion reactions.
- The most accessible and widely studied fusion reaction involves the isotopes of hydrogen, deuterium (D) and tritium (T). Deuterium is a naturally occurring isotope of hydrogen that can be extracted from seawater and is relatively abundant. On the other hand, tritium is not found in significant quantities in nature and needs to be produced. The production of tritium typically involves nuclear reactions with lithium. Enriched lithium (^{6}Li) can be irradiated with neutrons in a nuclear reactor or by using other particle sources to induce nuclear reactions. The resulting reactions lead to the production of tritium. The use of deuterium and tritium in fusion reactions offers several advantages. The deuterium-tritium (D-T) reaction has a relatively high reactivity and can release a significant amount of energy per reaction. It also operates at lower temperatures compared to other fusion reactions, making it more feasible for practical applications.

I.1. Fusion reactions in a reactor

In order to render fusion a usable energy source, additional parameters must be met. The plasma inside the reactor is never totally isolated and is subject to numerous losses, mainly through radiation. In order to define said losses, we refer to the energy confinement time (τ_E) which defines the amount time it takes for the plasma to lose all of its energy in the event all external energy sources are cut off. The Lawson criterion allows us to calculate if a fusion reactor would be energetically viable as the reactor must compensate for these losses:

$$n \cdot \tau_E > g(T) \cdot f(Q)$$

This condition imposes a limit which is less than the product of τ_E (energy confinement time) and n (particle density). For a fusion reaction to be self-sustaining (Q = 1), the product of the plasma density and energy confinement time ($n \cdot \tau_E$) must be greater than the product of the energy loss rate function (g(T)) and the fusion power multiplication factor (f(Q)).

The Q factor is often referred to as the energy amplification factor (gain) where Q = 1 indicates the power produced by the plasma is equal to the power required to sustain the reaction (external power), the breakeven point. Additionally, when Q = ∞, the plasma is self-sustaining as there is no external power being contributed to the reaction, the plasma is said to be in ignition.

As such, for a deuterium-tritium plasma, the function f(Q) can be approximated to 1, when the multiplication factor Q, is equal to 1. As Q increases, f(Q) quickly approaches a value of 5. Given these conditions, along with a temperature of 10 keV, the Lawson criterion can be expressed as follows:

$$n \cdot \tau_E \approx 10^{20} (m^{-3} \cdot s)$$

In Figure 2, we observe the different kinds of plasmas in astrophysics, solar physics, solid state physics, nuclear physics, and for technical applications, in a plot of electron temperature (eV) vs. electron density (cm^{-3}). The green line denotes the limitation of nonrelativistic plasmas, degenerate and non-ideal plasmas are positioned right from the blue and red lines, respectively.

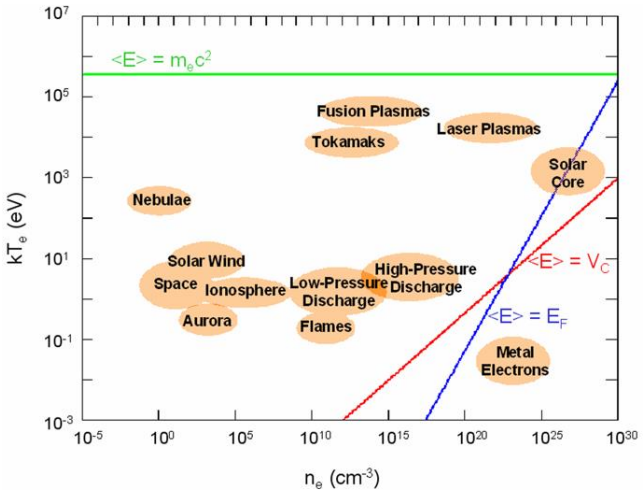

Figure 2: Different Kinds of Plasmas [2]

One can observe that the plasmas that are created by a fusion reactor are some of the hottest known plasmas. Additionally, this figure demonstrates the key difference between fusion found in stars versus that in fusion reactors, electron density. This is attributed to the fact that technological progress has yet to reach a point where we can produce the immense pressures required, hence, we compensate by elevating the plasma to a higher temperature.

Plasma is a conductive fluid that appears electrically neutral from the outside, where ions and electrons move almost independently. When immersed in a magnetic field, ions and electrons follow helical paths, winding around the field lines and being compelled to move along the field. This principle is known as magnetic confinement.

Additionally, plasma exhibits gas-like behaviour, generating kinetic pressure that pushes outward. This pressure increases with temperature and density. To confine the plasma effectively, an inward pressure must counterbalance the outward pressure. This is accomplished through the magnetic pressure exerted by the magnetic field.

In practical terms, to prevent instabilities, the kinetic pressure must be significantly lower than the magnetic pressure by a factor of 10. As a result, a density limit is imposed for a given magnetic field and temperature. For standard temperature (10-20 keV) and magnetic field (5-10 T) values, this density limit is approximately on the order of $10^{20}m^{-3}$.

Consequently, the required confinement time for magnetic fusion, as defined by the Lawson criterion, is on the order of a few seconds. This density limitation and confinement time play a crucial role in achieving stable and sustained fusion reactions.

The stability of the plasma is often assessed using the parameter β_n, which depends on plasma topology (such as aspect ratio and shape of the poloidal section), as well as current and pressure profiles. In current configurations, β_n typically ranges from 2.5% to 3.0%, while more advanced configurations can reach 5.0%. This parameter serves as a characterization of the stability limit in fusion systems.

Initially, straight or cylindrical configurations were explored, however, they had a drawback of allowing plasma to escape at the ends. To overcome this, the cylinder was closed upon itself, forming a torus shape characterized by the aspect ratio, which is the ratio of its major radius to its minor radius as shown in Figure 3.

However, in this toroidal configuration, two issues arise: the curvature of the field lines creates a centrifugal force, and the field's strength is non-uniform (stronger on the inner surface of the torus than the outer surface). These factors result in a drift of charged particles, where ions and electrons separate, with some moving to the top and others to the bottom, eventually escaping the magnetic confinement.

To counteract this drift effect, the field lines were modified to become helical. As a result, particles successively cross the top and bottom of the magnetic configuration, compensating for the consistent drift in the same direction. This is accomplished by introducing an additional magnetic field, known as the "poloidal" field, perpendicular to the toroidal field. The combination of these fields generates helical field lines, ensuring better particle confinement.

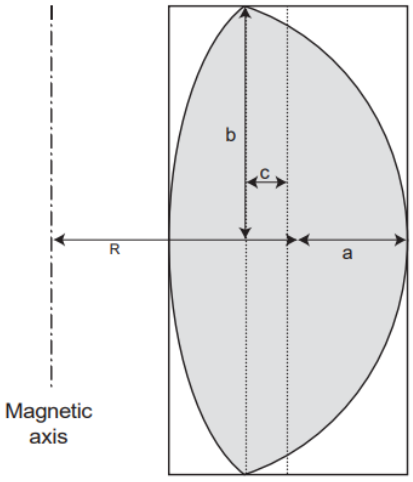

R: major radius
a: minor radius
A = R/a = aspect ratio
b/a = elongation
c/a = triangularity

Figure 3: Cross Section of the Main Geometrical Properties of a Torus [1]

As such, implementation of helicoidal field lines gives rise to two types of machines used in fusion research and technology, the tokamak and the stellarator. In a tokamak, the poloidal magnetic field is generated by an axial current flowing within the plasma itself. This magnetic field acts as the secondary circuit of a large-scale transformer, making the tokamak operate as a pulsed device as shown in Figure 4.

On the other hand, a stellarator's magnetic configuration relies entirely on currents circulating within external helical coils. This configuration, due to its more intricate principles and geometry, has progressed at a slower pace compared to the tokamak configuration. However, the stellarator configuration possesses certain inherent qualities, such as reduced dependence on plasma current, that have motivated ongoing research and development in this field.

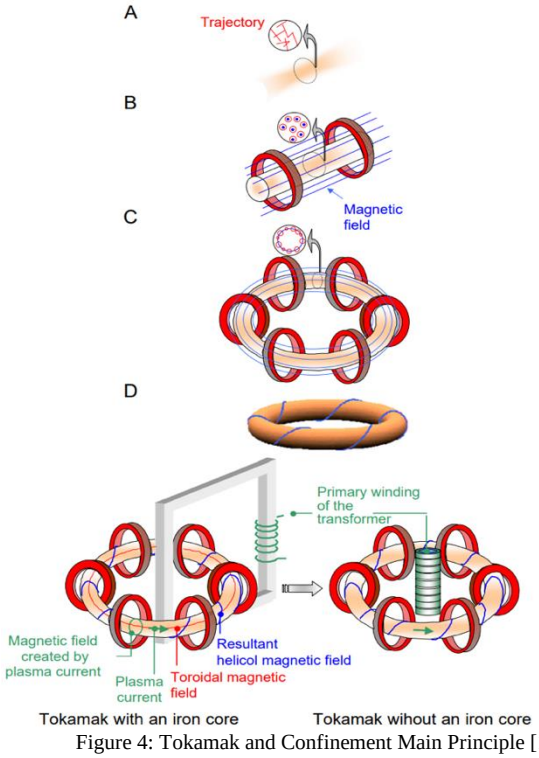

Figure 4: Tokamak and Confinement Main Principle [1]

I.2. Plasma heating

Regardless of the method used to create plasma within a confinement structure, it does not initially reach the temperature required for fusion reactions. There are three primary methods available for heating plasma. In a tokamak, the plasma is heated by the current circulating within it, which generates heat through the Joule effect. This method is effective up to temperatures of around 1 keV. Beyond this temperature, the plasma's resistivity becomes too weak, and this heating method becomes significantly less efficient. In contrast, in a stellarator, where there is no central current, there is no ohmic heating.

Additionally, neutral beam heating involves the injection of high-energy neutral particles into the plasma. These particles are created and accelerated outside the confinement containment. Before entering the plasma, the beam is neutralized through charge exchange. Once inside the plasma, the neutral particles become ionized again and are confined by the magnetic field. Through collisions, the energy is redistributed, leading to an increase in the plasma temperature.

Finally, plasma can absorb energy from electromagnetic waves at specific frequencies. Antennas located within the confinement area transfer the energy of electromagnetic waves to the plasma. By selecting the appropriate frequency, it is possible to target the heating of specific particle species (ions or electrons) and control the area where the wave energy is absorbed.

In a magnetic confinement-type thermonuclear fusion reactor, a combination of these heating methods is typically employed to raise the plasma temperature to the required level. Once a sufficient number of fusion reactions occur, the energy contributed by the helium nuclei produced within the plasma becomes the main heating method, contributing to the overall energy balance (referred to as $Q>5$).

In addition to their role in heating the plasma, the aforementioned heating methods have the capability to generate current. This feature opens up the possibility of envisioning continuous operation for the tokamak, despite its inherent pulsed nature.

Under certain conditions, the plasma can generate a toroidal current known as the bootstrap current. This current arises from collisions between circulating electrons and locally trapped electrons within the plasma. The contribution of the bootstrap current to the total plasma current strongly depends on the temperature and density profiles of the plasma.

The development of robust plasma scenarios that promote the generation of the bootstrap current is crucial for achieving steady-state operation, which is a fundamental requirement for future commercial fusion reactors. It involves optimizing various factors such as maintaining favourable temperature and density profiles, determining the appropriate locations for heat application, and effectively generating the desired current.

Efforts to establish reliable plasma scenarios that enhance the bootstrap current are of utmost importance as they contribute to the long-term sustainability and viability of commercial fusion power systems.

II. Fusion reactor analyses

After reviewing the principles of fusion energy and its important aspects in section I, our focus is lead to a deeper understanding of reactor design by analysing advancements in experimental fusion devices, such as ITER *(International Thermonuclear Experimental Reactor)*, SPARC, W7-X *(Wendelstein 7-X)*, NIF (*National Ignition Facility*), JET (*Joint European Torus*), JT-60U (*Japan Torus-60 Upgrade*) and TFTR (*Tokamak Fusion Test Reactor*). Our focus will mainly be oriented towards ITER and SPARC, as they provide the greatest source of most up-to-date information on their EDA (Engineering Design Activities) and their designs features the latest physical breakthroughs.

II.1. ITER's design phase

The origins of the ITER project can be traced back to 1978 when the European Commission, Japan, United States, and USSR came together for the International Tokamak Reactor (INTOR) Workshop. This collaborative effort, conducted under the auspices of the International Atomic Energy Agency (IAEA), aimed to evaluate the readiness of magnetic fusion for progressing towards the experimental power reactor (EPR) stage. The workshop also aimed to identify the necessary additional research and development (R&D) and define the characteristics of an EPR through a conceptual design.

Over the course of the late 1970s to the mid-1980s, numerous fusion scientists and engineers from each participating country dedicated themselves to an extensive assessment of tokamak confinement systems and potential designs for harnessing nuclear fusion energy. *"The overall programmatic objective of ITER is to demonstrate the scientific and technological feasibility of fusion energy for peaceful purposes. ITER would accomplish this by demonstrating controlled ignition and extended burn of deuterium-tritium plasmas, with steady state as an ultimate goal, by demonstrating technologies essential to a reactor in an integrated system, and by performing integrated testing of the high-heat flux and nuclear components required to utilize fusion energy for practical purposes."*[3]

In 1985, during the Geneva summit meeting, Mikhail Gorbachev proposed to Ronald Reagan that both countries undertake the joint construction of a tokamak EPR, aligning with the INTOR Workshop's proposal. This proposition ultimately led to the initiation of the ITER project in 1988, marking a significant milestone in the pursuit of fusion energy.

The purpose of ITER was based on the fact that the leading previous fusion experiments such as JET, JT-60U and TFTR, have realized their full performance potential, producing fusion power of 10-16 MW [4, 5], achieving equivalent break even condition [6] and investigating operation modes which may lead to a steady-state operation in ITER. [7]

In 1992, the detailed technical objectives to achieve the overall programmatic objective of ITER were adopted by all parties [8]. This demonstrated that ITER will undergo two distinct phases of operation, each spanning approximately ten years: the Basic Performance Phase (BPP) and the Enhanced Performance Phase (EPP). The primary focus of the initial phase, BPP, will be to address crucial challenges such as controlled ignition, extended burn, steady-state operation, and the testing of blanket modules.

Achieving these technical objectives necessitates demonstrating controlled ignition and extended burn in inductive pulses characterized by a flat-top duration of around 1000 seconds, accompanied by an average neutron wall loading of approximately 1 MW/m². Additionally, ITER should strive to showcase steady-state operation utilizing non-inductive current drive under conditions relevant to a reactor.

During the first phase, it is assumed that there will be a sufficient supply of tritium from external sources to facilitate the required experiments. The second phase will primarily focus on enhancing overall performance while conducting an extensive program for higher fluence components and materials testing, as such, tritium breeding may be implemented during this phase to explore its potential. Additionally, it will be essential for ITER to be designed in a manner that demonstrates the safety and environmental acceptability of fusion as a viable energy source.

The original Engineering Design Activities (EDA) of ITER were completed by the Parties in July 1998 after 6 years of activities. During this period,

Canada and Kazakhstan were also involved in the Project, with Canada associating with Europe and Kazakhstan with Russia. However, in 2003, Canada opted to withdraw from the project due to various reasons beyond the scope of this study.

Nonetheless, following the completion of the EDA, the Parties agreed to produce a detailed, complete, and fully integrated engineering design of ITER, along with all the necessary technical data for making decisions on its construction. The results of the EDA were made available to the Parties for international collaboration or utilization within their domestic programs. The deliverables at the end of the EDA met the original plan, and the ITER design, supported by technology R&D, reached an advanced stage of maturity with sufficient technical information for the construction decision.

Due to the delay in the construction decision, a three-year extension of the EDA was foreseen. During this extended period, specific design adaptations and safety analysis for sites, preparation of license applications, prototype testing, further physics studies, and the preparation of procurement documents were planned.

In a significant development, Canada rejoined the ITER project in 2020 after a seventeen-year hiatus. This renewed participation aimed to contribute to the complete realization of ITER, including the development of proposals and supporting information, such as a draft agreement for construction and operation.

However, during the course of the project, increasing financial constraints posed challenges in securing commitments to finance the construction effort at the originally agreed costs. Consequently, the Parties began seeking cost reduction measures while maintaining acceptable performance levels. A Special Work Group comprising representatives from the Parties was established to explore potential changes to the original technical objectives and develop new technical requirements that would align with the overall program objectives of the ITER EDA Agreement while minimizing costs. The amended technical guidelines are as follows:

Engineering Performance and Testing:

- Demonstrate availability and integration of essential fusion technologies;
- Test components for a future reactor;
- Test tritium breeding module concepts.

Plasma Performance:

- Extended burn in inductively driven plasmas at Q>10 for a range of scenarios;
- Aim at demonstrating steady-state through current drive at Q>5;
- Controlled ignition not precluded.

The newly proposed requirements align with the integrated "one-step" strategy towards DEMO, which has received approval from the Parties at the ITER Council [9]. The Council has requested the establishment of option(s) that minimize costs, targeting approximately 50% of the direct capital cost of the current design. These options would involve reduced detailed technical objectives while still satisfying the overall program goals of ITER. Furthermore, the utilization of existing design solutions and associated research and development efforts is encouraged.

The original plan encompassed careful considerations of various factors, including physics requirements for plasma confinement, control, and stability based on the ITER Physics Basis and Physics Rules [10]. In addition, engineering constraints such as heat loads, electromagnetic and mechanical characteristics, neutron shielding, and maintainability were thoroughly studied to ensure safe and reliable operation while maintaining reasonable costs. The main parameters, summarized in Table I, were defined based on this comprehensive analysis, with k_{95} representing the vertical elongation at 95% flux surface and δ_{95} representing the triangularity at 95% flux surface.

Total Fusion Power	1.5 GW
Auxiliary Heating Power	100 MW
Neutron Wall Loading	1 MW/m^2
Plasma Major Radius	8.1 m
Plasma Minor Radius	2.1 m
Plasma Current	21 MA
Toroidal Field @8.1 m Radius	5.7 T
Toroidal Field Coil	12 T
k_{95}	1.6
δ_{95}	0.24
Divertor Configuration	Single Null

Table 1: Dimensions and Parameters of ITER

The plasma performance of ITER is assessed based on the most recent experimental results and modelling available at the time, representing the best

information at that stage. The three key factors that directly influence plasma performance are as follows:

- Energy confinement, edge parameters, and the capacity to reach and sustain the H mode;
- The ratio of plasma pressure to magnetic field pressure (β) and particle density (n);
- Impurity dilution, radiation losses, helium exhaust, and divertor power handling.

Thorough studies of these issues have been conducted within a collaborative framework of voluntary ITER physics activities. Expert Groups have coordinated these efforts, leveraging the collective expertise in fusion programs across the participating Parties. The findings and insights are summarized in the ITER Physics Basis and Physics Rules [9].

Based on these results, the performance of ITER and its nominal operational range have been extensively investigated. Figure 5 (a) and (b) provide a summary, plotting fusion power as a function of the H-mode enhancement factor (H_H) for a 21 MA discharge. This factor characterizes the global energy confinement time relative to its reference extrapolated value based on ELMy H-mode confinement. The plots consider critical parameters such as power loss (P_{loss}) across the separatrix normalized by L-H power thresholds (P_{LH}), particle density (n) normalized by Greenwald density (n_{GW}), and normalized beta (β_N). They indicate the operational domain where three conditions, $P_{loss}/P_{LH} > 1$, $n/n_{GW} < 1.5$, and $\beta_N < 2.5$, are satisfied, either in an ignited condition (Figure 5 (a)) or in driven mode with heating power P_{aux} = 100 MW (Figure 5 (b)).

When in ignition, the available range of operational parameters around their normal values accounts for possible uncertainties in the extrapolation of confinement time. For driven modes, the feasible region extends to cover a broader range of uncertainties.

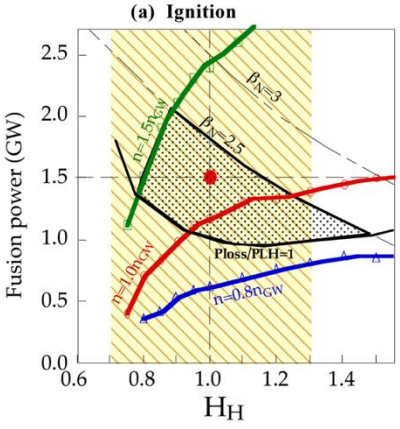

Figure 5 a: Fusion Power Domain at 21 MA – Ignition

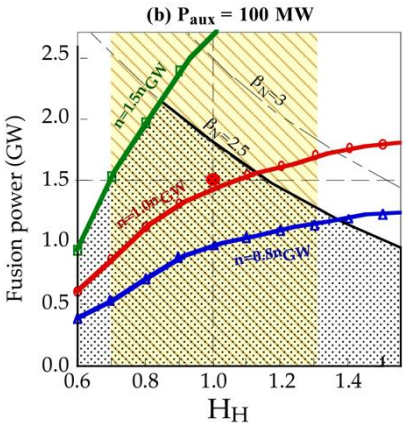

Figure 5 b: Fusion Power Domain at 21 MA – P_{aux} = 100 MW

The results of dynamic analysis and simulations demonstrate the simultaneous fulfilment and control of time-dependent requirements for plasma operation, including low divertor heat loads, helium pumping, and H-mode power thresholds. The design comprehensively incorporates all necessary provisions to ensure the reliable operation and control of ignited or high Q driven-burn deuterium-tritium (DT) plasmas, with fusion powers ranging from 1 GW to 1.5 GW and fusion burns ≥ 1000 s. The selection of nominal plasma parameters is based on "reference" physics basis assumptions, encompassing attainable energy confinement, plasma density, divertor target heat load, and projected plasma impurity content. This design enables sustained D-T burn with power equal to or exceeding 1 GW.

For the initiation of ignited burn and the sustainment of high-Q (≥10) driven burn, the design provides auxiliary heating and/or current drive powers of up to 100 MW. The in-vessel plasma-facing surfaces and nuclear shielding modules are specifically designed to handle steady-state power requirements. The Poloidal Field coil system is appropriately sized and configured to facilitate static and dynamic control of plasma equilibrium at plasma currents of up to 24 MA. It also supplies sufficient inductive current drive to generate nominal 21-MA, 1600-s duration pulses, including a 1000-s fusion burn. Additionally, somewhat shorter duration pulses (500-s burn) sustained by inductive methods at 24 MA are achievable. The design allows for the extension of controlled burn duration up to approximately 6000 s in a reduced-current driven-burn mode. Furthermore, a true steady-state plasma operation with current driven by non-inductive methods, within the 1 GW fusion power range and a reverse shear configuration, is also feasible.

The essential engineering features of the tokamak core include an integrated structural arrangement that links superconducting magnet coils (20

cased toroidal field coils, 9 poloidal field coils, and a monolithic central solenoid) with the vacuum vessel. This arrangement simplifies the equilibration of electromagnetic loads under all conditions, primarily relying on the robustness of the strong toroidal field coil cases (refer to Figure 7). In-vessel components, such as blanket modules on the back-plate and divertor cassettes (shown in Figure 6), are modular in design to facilitate safe and efficient maintenance through a combination of remote handling and hands-on techniques. The tokamak itself is housed within a cryostat vessel, located in an underground pit, and contained within a building with a height of approximately 50 m (refer to Figure 7). Table 2 provides a summary of the key engineering features of the design.

Peripheral equipment, including fuelling and pumping systems, heat transfer systems, auxiliary heating systems, and remote handling facilities, are arranged in galleries surrounding the main pit.

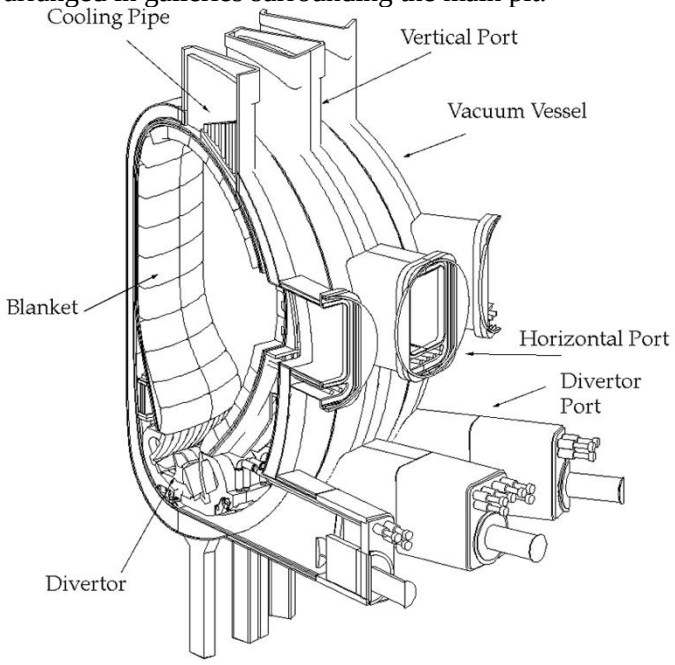

Figure 6: Isometric View of Vacuum Vessel, Blanket and Divertor [11]

In the event of seismic ground peak acceleration exceeding 0.2 g, additional isolation measures are implemented (as shown in Figure 8), creating a seismic gap at the pit wall and establishing an isolated "tokamak pit" with a diameter of 64 m. This pit is supported by flexible bearings, allowing substantial horizontal movement (approximately 200 mm) while maintaining vertical stability. This design concept minimizes the need for significant modifications due to variations in seismic conditions. The main services required for ITER, such as electrical power, cooling water, fuel treatment, information flow, assembly and maintenance facilities, and waste treatment, are distributed among ancillary buildings and other structures throughout the approximately 60-hectare site.

Super Conducting Toroidal Field Coils (20 Coils)	
Superconductor	Nb_3Sn in circular Incoloy jacket in grooved radial plates
Structure	Pancake wound, in welded steel case
Maximum Field	12.5 T
Super Conducting Central Solenoid (CS)	
Superconductor	Nb_3Sn in square Incoloy jacket
Structure	Layer wound
Maximum Field	13 T
Super Conducting Poloidal Field Coils (PF 1-9)	
Superconductor	NbTi in square Stainless-Steel conduit
Structure	Double pancakes
Maximum Field	5 T (PF 1~8), 6.7 T (PF 9)
Vacuum Vessel	
Structure	Double-wall welded ribbed shell, with internal shield plates and ferro-magnetic inserts
Material	Stainless Steel 316 LN structure, SS 304 with 2% boron shield, SS 430 inserts
1st Wall/Blanket (Basic Performance Phase)	
Structure	Armor-faced modules mechanically attached to toroidal backplate
Materials	Be armor Copper alloy heat sink Stainless Steel 316 LN structure
Divertor	
Configuration	Single null 60 solid replaceable cassettes
Materials	W alloy and C plasma facing components Copper alloy heat sink Stainless Steel 316 LN structure
Cryostat	
Structure	Ribbed cylinder with flat ends
Maximum Inner Dimensions	36 m diameter, 30 m height
Material	Stainless Steel 304L
Heat Transfer Systems (Water-cooled)	
Heat Released In The Tokamak During Nominal Pulsed Operation	2200 MW at ~ 4 MPa water pressure, 150°C
Cryoplant	
Nominal Average He Refrigeration/ Liquefaction	120 kW/0.25 kg/s

Rate For Magnets And Divertor Cryopumps (4.5 K)	
Nominal Cooling Capacity At 80 K	510 kW
Additional Heating And Current Drive	
Total Injected Power	100 MW
Candidate Additional Heating And Current Drive (H&CD) Systems	Electron Cyclotron, Ion Cyclotron, Lower Hybrid, Neutral Beam from 1 MeV negative ions
Electrical Power Supply	
Pulsed Power Supply From Grid Total Active/Reactive Power Demand	650 MW/500 Mvar
Steady-state Power Supply From Grid Total Active/Reactive Power Demand	230 MW/160 Mvar

Table 2: Summary of Key Engineering Features of ITER's Design [11]

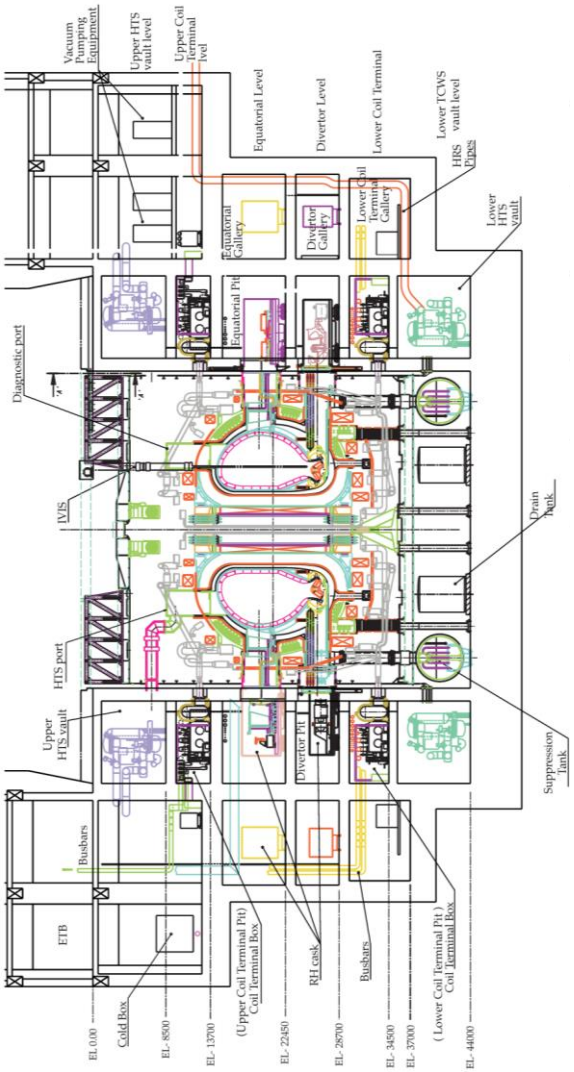

Figure 7: Elevation View of ITER's Equipment Layout [11]

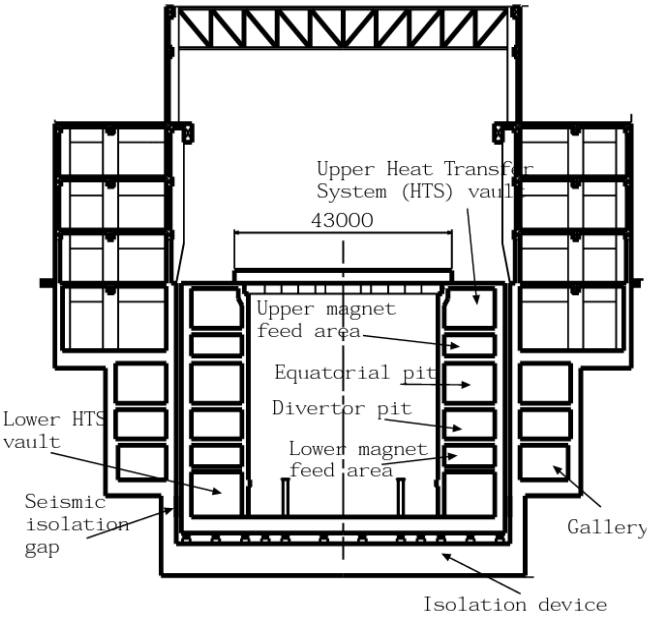

Figure 8: ITER's Tokamak Building and Pit [11]

II.2. ITER's Implementation Phase

The guiding principle behind the design of ITER has been to employ proven methodologies and verify their suitability for ITER through meticulous analysis, as well as through the construction and examination of extensive, full-scale models and prototypes of the essential systems.

We will now analyse how ITER was implemented outside of the design phase, starting with highlighting ITER's major technical challenges, listed below:

- Unprecedented size of the superconducting magnet and structures
- High neutron flux and high heat flux at the first wall/shield blanket
- Extremely high heat flux in the divertor
- Remote handling for maintenance/intervention of an activated tokamak structure
- The first fusion machine with a large radioactive inventory
- Unique equipment for fusion reactors such as fuelling, pumping, heating/current drive system, diagnostics, etc.

To facilitate the comprehensive technology research and development necessary for validating the crucial aspects of the design, ITER's technology R&D efforts were concentrated on seven major projects, with each project dedicated to a specific key aspect. Two of these projects are dedicated to advancing

superconducting magnet technology. The Central Solenoid (CS) Model Coil Project and the Toroidal Field (TF) Model Coil Project aim to develop the full-scale conductor for ITER magnets, including strand, cable, conduit, termination, and related R&D on AC losses, stability, and joint performance. These projects involve collaboration between multiple teams to produce scaled model coils and associated mechanical structures. The production and qualification of 29 tons of Nb3Sn strand from various suppliers have been successfully completed. Significant progress has also been made in cabling, jacketing, winding, and heat treatment processes for both the CS and TF model coils.

In addition to magnet technology, three projects concentrate on key in-vessel components. The Vacuum Vessel Sector Project focuses on producing a full-scale sector of the ITER vacuum vessel, establishing tolerances, and conducting initial mechanical and hydraulic performance tests. Key technologies and manufacturing techniques have been established, and two full-scale vacuum vessel segments have been completed within the required tolerances. The Blanket Module Project aims to produce and test full-scale modules of primary wall elements and prototypes of coolant manifolds and backplates. Successful development, testing, and qualification of material interfaces have been achieved, and a full-scale model without attached components has been completed. The Divertor Cassette Project focuses on building a divertor capable of withstanding high thermal and mechanical loads during normal operation and transients. Full-scale prototypes of half-cassettes are being built and subjected to heat flux and mechanical tests.

The last two large projects within ITER focus on remote handling technologies. The goal is to develop tools and facilities for remote interventions in contaminated and activated conditions, ensuring flexibility while meeting safety and environmental requirements. The Blanket Module Remote Handling Project demonstrates the remote replacement of ITER Blanket modules, including transport scenarios, vacuum vessel operations, and the use of a monorail-based transport vehicle. Full-scale equipment and tools have been fabricated, and integrated tests are underway in a Blanket Test Platform. The Divertor Remote Handling Development project aims to demonstrate the remote removal and refurbishment of ITER divertor cassettes. Full-scale prototype remote handling equipment and tools are being designed, manufactured, and tested in dedicated test platforms simulating the divertor area and refurbishment facility.

Once the individual projects were completed, the technical output from R&D validated the technologies and confirmed the manufacturing techniques and quality assurance (QA) incorporated in the ITER Design. It also supported the manufacturing cost estimates for important key cost drivers.

Analysing the operational plan of ITER, one can observe that ITER will have 3 main operation phases, the Basic Performance Phase (BPP), the Transient Phase, and the Enhanced Performance Phase (EPP).

The Basic Performance Phase of ITER, spanning a duration of 10 years, involves a systematic progression towards achieving fusion power. The operations will proceed in a step-by-step manner, beginning with hydrogen plasma operation characterized by low plasma current, low magnetic field, short pulse duration, and a low duty factor. Fusion power will not be generated during this initial phase. The primary objective is to validate plasma characteristics and minimize uncertainties before advancing to subsequent stages.

During the initial 2.5 years, hydrogen plasma experiments will be conducted without any fusion reactions taking place. Additionally, the in-vessel components of ITER will remain inactive, ensuring they are not contaminated by tritium. This non-activated state allows for the commissioning of ITER, where tokamak discharges will be performed at maximum plasma current and magnetic field. A reliable scenario for plasma operation, enabling the achievement of the maximum plasma current, will be developed. This phase can be referred to as the prenuclear commissioning phase.

Following the prenuclear commissioning phase, deuterium plasma experiments will commence, utilizing a limited amount of tritium. The final commissioning of ITER will take place, with particular emphasis on assessing the shielding performance. Gradually, fusion power and pulse length will be increased, ensuring a safe and dependable operation of ITER.

By the fifth year, the goal is to attain a reference operation with a burn pulse of 1.5 GW and a duration of 1000 seconds. Simultaneously, various operation modes, including steady-state operation, will be explored and studied alongside the development of the reference operation. The plan for the Basic Performance Phase (BPP) is summarized in Table III.

Nearing the end of the Basic Performance Phase, the evaluation of ITER's tritium breeding blanket for the Extended Performance Phase (EPP), will commence. Specifically, tests will be conducted on blankets designed for the Demonstration Fusion Reactor (DEMO). The

Parties involved have planned to test four different tritium breeding blanket concepts relevant to DEMO, alongside one intended for the breeding blanket of ITER's Extended Performance Phase (EPP), responsible for producing a significant portion of tritium fuel. To accommodate these tests, ITER has allocated four equatorial ports specifically for tritium breeding blanket experiments.

The objective is to accumulate an average neutron fluence of up to 0.3 MWa/m² on the first wall during this phase. To meet this goal, an adequate external tritium supply is available. As the Basic Performance Phase (BPP) progresses over a period of 7.5 years, the net consumption of tritium will increase from 0.6 kg/year to 6.5 kg/year in the deuterium-tritium (DT) phase. This escalating consumption reflects the advancing stages of ITER's development.

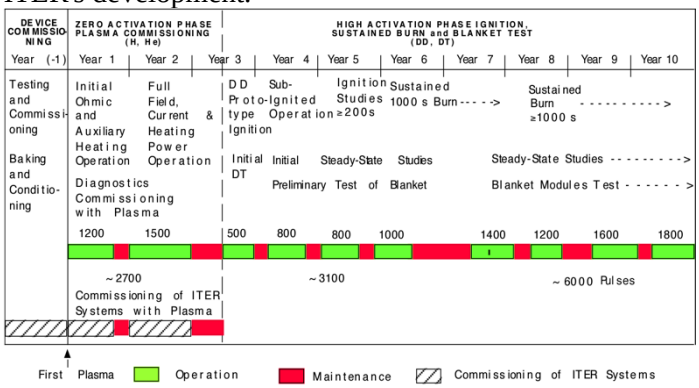

Table 3: ITER Plasma Operation Plan For The BPP [11]

During the Transient Phase spanning two years, the shielding blankets utilized in the Basic Performance Phase (BPP) will be substituted with breeding blankets. This replacement is necessary as the availability of external tritium resources is inadequate to support a substantially higher neutron fluence than that experienced in the BPP. The transition from shielding blankets to breeding blankets is estimated to take approximately two years to complete.

To sustain a ten-year operation, assuming an external supply of 1.7 kg of tritium per year, a tritium breeding ratio of around 0.8 would be satisfactory to achieve a neutron fluence of approximately 1 MWa/m². This fluence level is considered viable for extended operation, signifying the effectiveness of the breeding blankets in producing tritium.

The Transient Phase will serve as the crucial bridge between the Basic Performance Phase (BPP) and the subsequent Extended Performance Phase (EPP), enabling the necessary adjustments in blanket configurations to maximize tritium production while considering the available tritium resources.

Finally, the Enhanced Performance Phase (EPP), will have an anticipated duration of approximately ten years and does not currently have a fully defined operation plan. The plan for this phase will be determined based on the plasma performance and operational insights gained during the Basic Performance Phase (BPP). However, it is anticipated that the EPP will shift its focus from extensive physics studies to prioritizing the optimization of performance and ensuring reliable operation. This phase will aim to maximize neutron fluxes and fluences by employing the most promising operational modes developed and refined during the BPP.

The emphasis during the EPP will be on leveraging the knowledge and experience gained from the preceding phase to enhance overall performance and achieve higher levels of operational efficiency. By capitalizing on the lessons learned and advancements made in the BPP, the EPP will work towards refining operational parameters, improving plasma performance, and generating increased neutron fluxes and fluences.

The flexibility of the EPP's operation plan allows for adaptability based on the evolving understanding of plasma behaviour and the effectiveness of various operational modes. This phase will contribute significantly to the optimization and reliable operation of ITER, as it leverages the successes and lessons of the BPP while focusing on achieving enhanced performance and high neutron fluxes.

Plasma operation within ITER will firstly be based on inductive plasma operation, utilizing a reference plasma operation scenario known as saw-toothing ELMy H-mode operation. This scenario, commonly employed in current tokamaks with shaped-cross-section divertors, aims to sustain the required 21 MA current during the 1000-second burn phase using inductive current drive.

Figures 9 and 10 provide an illustration of the scenario concept, highlighting the evolution of plasma current, shape, and configuration, which are crucial elements within this scenario. The key features of the nominal plasma operation scenario include:

- A 530 Wb poloidal field (PF) system flux swing.
- Inductive plasma initiation, specifically through Townsend avalanche breakdown, with assistance from electron cyclotron (EC) heating. This occurs in a high-order multipole field null positioned near an outboard port-mounted startup/shutdown limiter.
- Expansion of the startup plasma's minor radius and elongation on the limiter before divertor formation at approximately 15 MA plasma current (*Ip*).

- Maintenance of a precisely-controlled single-null divertor plasma configuration during the heating, burn, and burn termination phases of the scenario. Plasma current termination is achieved by controlled contraction of the minor radius and elongation on the limiter.

Simulations of plasma startup and shutdown dynamics indicate that the required magnetohydrodynamic (MHD) stability and power balance at the plasma edge, necessary to avoid density limit disruptions, are satisfied with acceptable margins. The simulations also demonstrate that the plasma's resistive flux consumption during startup and current ramp-up falls within the design basis guideline of $0.45\mu_0 R_o I_p \approx 100$ *Wb*, with sufficient PF (≥80 Wb) system flux swing available to sustain the 21 MA plasma current during the fusion burn.

The nominal plasma operation scenario is designed for a reference case burn phase plasma with 21 MA plasma current (I_p), poloidal beta (b_p) of 0.9, and a dimensionless internal inductance ($l_i(3)$) of 0.9. The poloidal field coils and their power supplies are sized to enable plasma equilibrium control and achieve inductively-sustained burn durations of over 1000 seconds for 21 MA plasmas within the range of $0.7 \leq b_p \leq 1.2$ and $0.7 \leq l_i \leq 1.1$. Plasma operation with 24 MA plasma current (I_p) and corresponding parameters for 1.5 GW fusion power, such as b_p and l_i, is also feasible, with an inductively-sustained burn duration of approximately 500 seconds.

The scenario concept depicted in Figures 5 and 6 also supports ITER's initial plasma commissioning with ohmic and auxiliary-heated deuterium-deuterium (DD) plasmas. Furthermore, it enables extended-pulse inductively-sustained driven-burn operation with reduced plasma current (~6000 seconds burn at approximately 1 GW with I_p = 17 MA and 100 MW of auxiliary heating power).

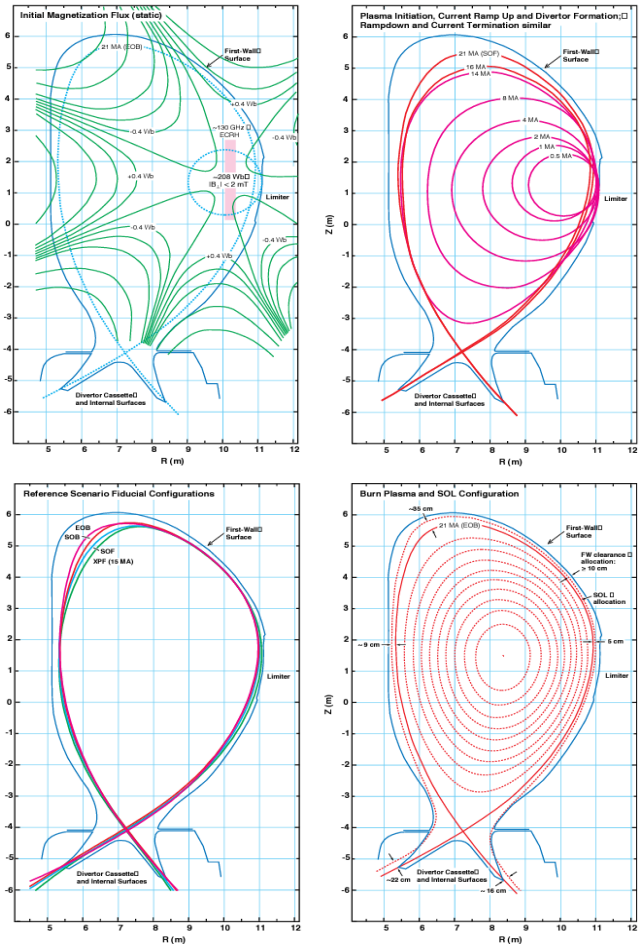

Figure 9: Plasma Configuration Evolution for 21 MA Operations

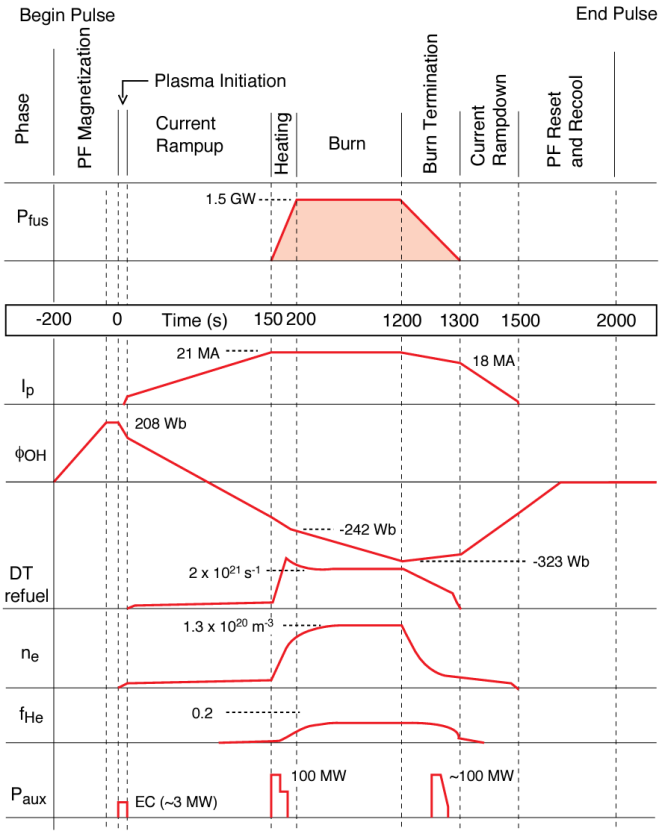

Figure 10: PF and Plasma Parameter Waveforms for 21 MA Operations

Following the inductive plasma operation phase, ITER will commence the steady-state and enhanced performance operation phase. The hardware provisions in ITER encompass sufficient flexibility in the poloidal field system and magnetic control capabilities to facilitate steady-state plasma operation sustained entirely by non-inductive current drive and bootstrap current. Feasibility assessments indicate that the present design of ITER aligns with the known requirements for reversed-shear plasma operation modes, which have been achieved in current tokamaks on a transient basis [14].

However, the full understanding of the physics basis and the necessary plasma operation features to achieve and control steady-state operation are ongoing subjects of physics research and development. Therefore, the extent to which steady-state operation can be realized in ITER and the specific details of how such operation will be controlled remain areas of future investigation.

Several considerations related to plasma operation and control in a reversed shear mode have emerged in relation to ITER. Firstly, the required reversed shear, characterized by weak or negative central magnetic shear ($s = r/q\ dq/dr$), can be readily produced in ITER using similar current and/or shape ramping techniques combined with early auxiliary heating methods employed in achieving enhanced performance reverse shear modes in existing tokamaks.

Secondly, the ITER poloidal field system and divertor system are compatible with generating and stabilizing a high-q, low-li, high-elongation, and high-triangularity plasma. This configuration can be achieved by shifting the plasma outward while reducing the minor radius. For example, an outward shift of approximately 0.5 m, with key parameters such as $R_o \sim 8.6$ m, $a \sim 2.35$ m, $I_p \sim 12$ MA, $q_{95} \sim 5$, $l_i \sim 0.4$, $k_{95} \sim 2.0$, and $d_{95} \sim 0.45$, can facilitate the desired plasma characteristics.

Thirdly, sustaining a suitable reverse-shear current profile and a non-inductive 12 MA current, along with approximately 9.5 MA of bootstrap current, is attainable through appropriate allocation of 100 MW of current drive power, distributed between on-axis and off-axis deposition.

These collective features support the notion that non-inductively sustained steady-state plasma operation in the 1 GW power range is achievable in ITER, provided that certain criteria are met. These criteria include the attainment of an energy confinement enhancement of approximately 1.3 times that of ELMy H-mode confinement and a high poloidal beta of approximately 2.3.

II.3. SPARC's design phase

SPARC is a compact (R_0=1.85m, a=0.57m), superconducting, high-field (B_0=12.2T) tokamak designed to achieve fusion gain (Q) greater than 2, marking a significant milestone in magnetically confined fusion plasma research. Currently in the design phase, SPARC builds upon the high-field trajectory established by the Alcator series of tokamaks, incorporating new magnets based on rare earth barium copper oxide high-temperature superconductors. This design choice aims to achieve exceptional performance within a compact device.

The primary objective of SPARC is to attain a fusion gain (Q) exceeding 2, based on conservative physics assumptions such as $H_{98,y2}$=0.7. With the nominal assumption of $H_{98,y2}$=1, SPARC is projected to reach a fusion gain (Q) of approximately 11 and a fusion power (P_{fusion}) of around 140 MW. These ambitious goals position SPARC as a unique platform for advancing burning plasma physics research. It will operate at high plasma density ($n_e \approx 3\times10^{20}$m^{-3}), high temperature ($T_e \approx 7$keV), and high-power density ($P_{fusion}/V_{plasma} \approx 7$MWm^{-3}), which are key parameters relevant to future fusion power plants.

SPARC's innovative design, utilizing high-temperature superconductors and operating at high magnetic fields, offers promising prospects for achieving significant advancements in fusion energy research.

The SPARC project encompasses two central mission objectives. Firstly, it aims to achieve a fusion gain (Q) greater than 2, surpassing the critical threshold for fusion energy production and marking a significant advancement on the path towards commercial fusion energy. By exceeding this goal and achieving higher gains, SPARC will also address various innovative challenges in burning plasma research. These challenges include burn control, self-organization of burning plasmas, interactions between alpha particles and magnetohydrodynamic (MHD) modes, divertor physics, and the prediction and mitigation of disruptions.

Secondly, SPARC seeks to demonstrate the viability of rare earth barium copper oxide (REBCO) high-temperature superconducting (HTS) magnets within an integrated fusion confinement facility. This demonstration will pave the way for future power plants utilizing this technology, such as the ARC power plant concept. By utilizing REBCO-based magnets, SPARC aims to showcase the advantages of high magnetic fields, enabling the reduction in size of fusion devices and facilitating rapid progress at lower costs.

The SPARC project aspires to not only achieve significant scientific milestones but also lay the foundation for future fusion power plants. By demonstrating successful fusion gain and the potential of REBCO HTS magnets, SPARC contributes to the advancement of fusion energy research and the potential realization of economically viable and sustainable fusion power generation.

Since the early days of fusion research, significant progress has been made in the science and technology of tokamaks. Milestones were consistently achieved, with new records set in the triple product, a key metric for plasma performance, every few years. Notably, TFTR and JET further propelled advancements by not only setting records in the triple product but also in D-T fusion gain. However, progress in this regard has largely stagnated since the 1990s. While the field of plasma physics and fusion has advanced considerably during this time, the record fusion gains from TFTR, JET, and the D-T equivalent performance in JT-60U still stand unchallenged even after many years.

To understand the reasons behind this delay in progress, it is necessary to examine the primary factors contributing to the increase in the triple product or fusion gain. As outlined in the ITER Physics Basis, the Progress in the ITER Physics Basis, and other relevant literature, there are primarily three avenues through which fusion performance can be improved.

The first approach involves the discovery of new operating regimes, such as the significant breakthrough of H-mode discovery or finding ways to overcome known physical limitations. The second approach is to increase the magnetic field strength of the fusion device. Lastly, one can aim to enlarge the physical size of the machine itself. In the absence of new physics discoveries, achieving higher fusion performance heavily relies on either increased magnetic field strength or an increase in the size of the device.

While advancements in these areas have contributed to progress in the past, finding innovative solutions and pushing the boundaries in these aspects remains crucial for achieving further breakthroughs in fusion energy research.

Figure 11 illustrates the relationship between the achievable fusion gain (Q), the toroidal field on the axis (B_0), and the major radius (R_0). The calculations in Figure 11 consider various parameters such as shaping (κ_a=1.75 and δ_{sep}=0.54), q*=3.05, impurity content, $H_{98,y2}$=1, and keeping the aspect ratio to 0.31, while limiting operation to below 0.9 normalized Greenwald density ($0.9n_G$). The fusion gain (Q) is calculated using empirical scaling methods, while keeping certain parameters constant. This plot allows for a comparison with specific design points of other machines, both existing and proposed, marked at their respective R_0 and B_0 values.

Despite differences in shaping and other parameters, the predicted or observed gains (or D-T equivalent gains) in most other machines align with the plotted Q contours, demonstrating the general relationship between B_0, R_0, and Q. The vertical dashed grey line represents the approximate on-axis field limit for machines utilizing Low-Temperature Superconductors (LTS). The plasma volume is indicated on the right vertical axis, providing an indicator of the project scale.

It's important to note that this particular calculation focuses solely on core confinement and does not consider plasma exhaust, neutron loading, or engineering constraints. The gain is a nonlinear function of both the field and size. By increasing the field, one can decrease the size while maintaining the same gain without altering any physics assumptions. The good agreement between the Q contours in Figure 11 and predictions or observations from other machine design points emphasizes the general relationship between toroidal field, size, and gain. This underscores the motivation to

aim for the highest achievable field within technological constraints.

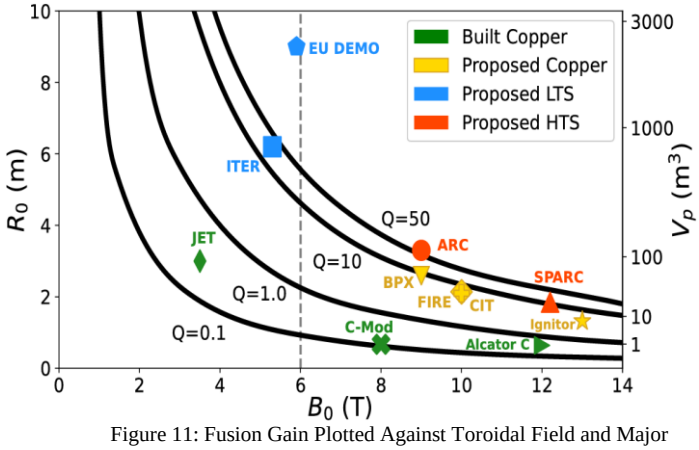

Figure 11: Fusion Gain Plotted Against Toroidal Field and Major Radius

During the design phase of ITER, the state-of-the-art superconductor was Nb_3Sn, and the practical achievable magnetic field with available superconducting materials was limited to approximately 13 Tesla on the conductor. This, in a standard aspect ratio tokamak (≈0.3), limited the field on axis to around 5 or 6 Tesla. As shown in Figure 11, constraining the toroidal field to 5.3 Tesla required a major radius of approximately 6 meters to achieve a fusion gain (Q) of approximately 10. In this sense, ITER-FEAT was designed to be the smallest machine capable of achieving Q≈10 while respecting the technological limitations of magnetic field strength at that time. Unfortunately, the large size of the machine, along with associated costs, time requirements, and organizational challenges stemming from the scale of the project, have contributed to the slower progress in fusion gain over the past two decades. The pace and cost associated with such large and complex projects also raise concerns about the economic viability of a commercial power plant based on this approach. The current design point for the EU-DEMO is also shown in Figure 11. It should be noted that the shaping for EU-DEMO (and for ITER) is less than assumed in Figure 11, resulting in a projected performance of Q≈40 [15], which is lower than indicated.

Even during the design phase of ITER, it was acknowledged that without the constraint in magnetic field strength, it would be possible to construct a high-gain device that was much smaller. This sentiment is reflected in the designs of several high-field copper devices, such as CIT, BPX, FIRE, and Ignitor, which aimed to achieve high gain on a smaller scale compared to ITER. These devices followed the high-field trajectory of the Alcator series of tokamaks and pursued high gain while recognizing that their magnet technology would not be applicable in a power plant. Given the advancements since their design, it still appears likely that these machines would have achieved break-even (and possibly high gain) if they had been constructed. BPX, CIT, FIRE, and Ignitor are also shown in Figure 11 and fall along the Q≈10 curve.

In recent years, however, new high-temperature superconductor (HTS) materials have emerged as viable alternatives to older low-temperature superconductors (LTS). One of these materials, REBCO, has been recognized for its potential use in fusion magnets. With recent advancements, REBCO is now available in large quantities and offers high performance, allowing access to significantly higher magnetic fields than was possible with Nb_3Sn. This technological breakthrough opens up new possibilities for designing a superconducting tokamak with Q>1 (and the path towards a commercial power plant) while operating on the same physics basis as ITER but with different engineering constraints.

Parameter		ITER	SPARC	Ignitor	FIRE	BPX	CIT
R_0	m	6.2	1.85	1.32	2.14	2.405	2.1
A	m	2	0.57	0.47	0.6	0.8	0.65
ϵ		0.32	0.31	0.36	0.28	0.31	0.31
ϵ		0.32	0.31	0.36	0.28	0.31	0.31
B_0	T	5.3	12.2	13	10	9	10
I_p	MA	5	8.7	1.01	7.71	1.81	1
κ_{sepa}		1.85	1.97	1.83	2	2	2
δ_{sepa}		0.48	0.54	0.4	0.7	0.45	0.25
$P_{aux,max}$	MW	73	25	24	20	20	20
$\Delta t_{flattop}$	s	400	10	4	20	10	5
Φ_{tot}	Wb	277	42	33	43	77	75
P_{fusion}	MW	500	140	96	150	100	800
Q		10	11	9	10	5	∞

		C-Mod	AUG	DIII-D	EAST	KSTAR
R_0	m	0.67	1.65	1.66	1.7	1.8
A	m	0.21	0.5	0.67	0.4	0.5
ϵ		0.31	0.3	0.4	0.24	0.28
B_0	T	8	3.9	2.2	3.5	3.5
I_p	MA	2	1.6	2	1	2.01
κ_{sepa}		1.8	1.6	2.01	2	2
δ_{sepa}		0.4	0.5	0.75	0.6	0.8
$P_{aux,max}$	MW	6	30	27	28	16
$\Delta t_{flattop}$	s	1	10	6	1000	20
Φ_{tot}	Wb	8	9	12	10	17

Table 4: ITER and SPARC Compared to Other Reactors

With a major radius of 1.85 m and an inverse aspect ratio of 0.31, SPARC falls within the size and aspect ratio range of many present-day "medium-sized" tokamaks, such as DIII-D, ASDEX Upgrade, EAST, and KSTAR (as seen in table 4). However, SPARC benefits from a significantly higher toroidal field (12.2 T), which allows for a larger plasma current at the same safety factor and enables a significantly higher triple product compared to existing devices.

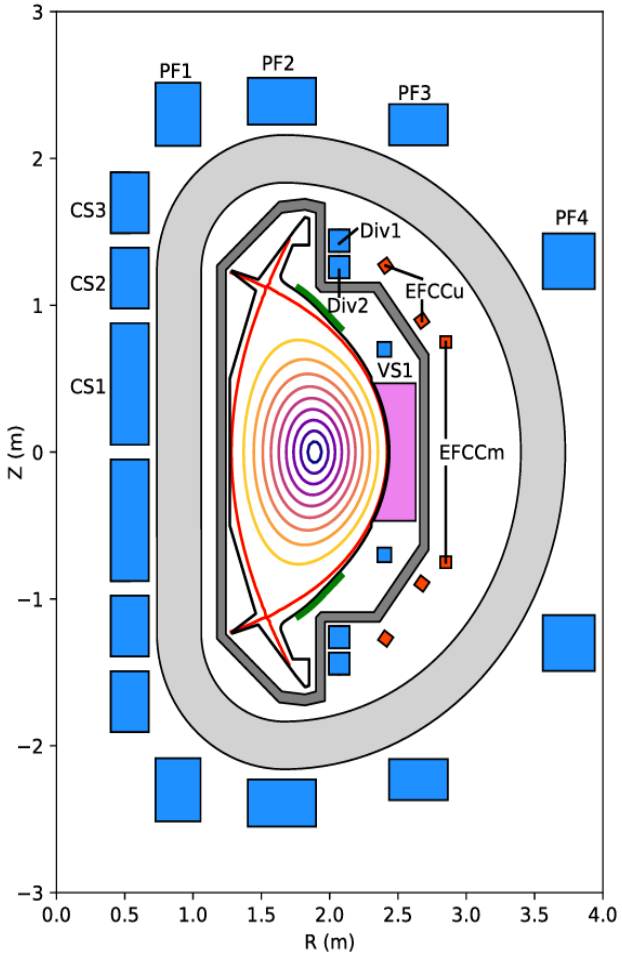

Figure 12: SPARC Poloidal Cross-Section

Figure 12 illustrates the poloidal cross-section of SPARC V2. The entire SPARC device is maximally up-down symmetric, facilitating tests of symmetric double-null operation. The central solenoid, consisting of three pairs of HTS upper and lower coils (CS1, CS2, and CS3), is depicted in blue. Outside the toroidal field coils, there are four pairs of HTS poloidal field coils (PF1 to PF4) moving outward in major radius. Additionally, there are two pairs of copper coils (Div1 and Div2) that are internal to the toroidal field coils but external to the vacuum vessel, primarily used for divertor magnetic field actuation. Inside the vacuum vessel, there is a pair of vertical stability coils (VS1 upper and lower). Lastly, three sets of picture-frame error-field correction coils, one upper, one lower, and one midplane, are present.

The vacuum vessel of SPARC is double-walled, with space between the walls for gas heating and cooling. Approximately half of the space between the vessel walls, as well as the space between the vessel and the toroidal field coils, is filled with neutron shielding material to reduce nuclear heating of the superconducting magnets. The vacuum vessel is equipped with three ports at each toroidal location, including one midplane port and an asymmetric pair of off-midplane ports located above and below.

The divertor in SPARC is designed to be toroidally continuous and tightly baffled to contain neutral particles within the divertor volume. Both carbon and tungsten are currently being considered as materials for plasma-facing components. In summary, carbon plasma-facing components would result in lower core impurity radiation and more forgiving divertor operation compared to tungsten. However, carbon components would also lead to increased tritium retention due to higher erosion and co-deposition rates. While tungsten-based plasma-facing components are believed to be more suitable for a power plant scenario [17], the relatively short integrated plasma time in SPARC allows for carbon to be considered as a viable option. Both materials are being examined.

Upper and lower passive stability plates are positioned between the vacuum vessel and the plasma to enhance vertical stability and enable operation at high elongation. SPARC incorporates 18 toroidal field coils in an effort to balance the competing constraints of minimizing magnetic field ripple and maximizing vacuum vessel port width. The design includes up to 25 MW of 120 MHz ion cyclotron resonance heating (ICRH) as the sole source of auxiliary heating for the plasma.

The central solenoid and poloidal field coil set have the capability to generate 42 Wb of magnetic flux to initiate and drive the plasma current, with a plasma flattop time of 10 s. All systems are designed to support full-power operation during the flattop phase. The compact size of SPARC allows for the achievement of a well-equilibrated plasma in a relatively short discharge duration (<10 s) compared to larger machines like ITER, which simplifies the design of many engineering systems. The predicted energy confinement time for SPARC is $\tau_E \approx 0.77$ s, indicating that the flattop phase encompasses more than 10 energy confinement times. Plasma current and safety factors were calculated using

the Tokamak Simulation Code (TSC) for the full-performance SPARC discharge. It was demonstrated that the current profile reaches a well-equilibrated state within approximately 5 s after the start of the flattop phase, and any further changes are primarily driven by sawtooth relaxation. This finding is consistent with more detailed time-dependent transport simulations predictions of core plasma performance for the SPARC tokamak [18].

The iterations of the SPARC design leading to V2 have involved a wide range of engineering analyses. Significant effort has been devoted to the structural, thermal, and electromagnetic analysis of the toroidal field coils, which represent a novel aspect of the SPARC design. Similar efforts have been undertaken for the central solenoid and poloidal field coils. The vacuum vessel has also been a key focus of the early design work as it interfaces with many other systems and must withstand large disruption loading. Since ICRH is the only external heating source, its design has also progressed considerably to ensure reliable power coupling to the plasma. Additionally, the effects of neutron heating have been modelled for the entire device, including determining the cooling requirements for the superconducting magnets during D-T operation. Given the high volume-averaged fusion power density and the tight radial build of SPARC, volumetric neutron heating of various components is of particular importance.

To ensure the achievement of the SPARC mission of fusion gain Q>2, several scenarios are being analysed to demonstrate both the feasibility of the mission and the necessary steps in the experimental research plan. Specifically, three operational scenarios are described here: a full-performance (full field, current, and shaping) H-mode discharge, a full-performance L-mode discharge, and a reduced field and current H-mode discharge.

The performance for these scenarios is estimated in a manner similar to that used for the initial design of ITER. Zero-dimensional scaling laws (energy confinement, L-H power threshold, density peaking, etc.) are combined with estimates of plasma profiles and assumptions about other properties of the core plasma in order to calculate the operational range of a machine with a given set of input parameters.

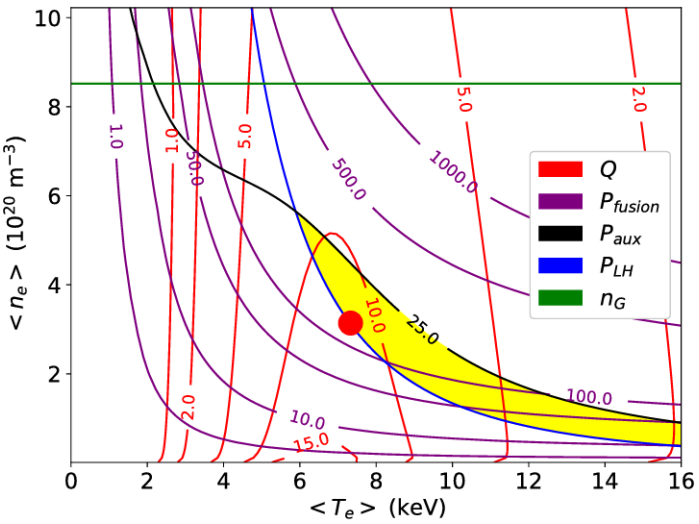

Figure 13: Plasma Operating Contour for Full-Field, Full-Current H-Mode Operation

These calculations were examined with Plasma Operating Contours (POPCONs), an example of which is shown in Figure 13 where the operational space of SPARC, depicted by the yellow shaded region, indicates the area where the power generated exceeds the L-H power threshold but remains below the available auxiliary heating power. The temperature and density values are averaged across the volume. Within this space, the operating point for the full-performance H-mode discharge is represented by the red circle. In addition to these empirical zero-dimensional projections, integrated modelling with physics-based models has been performed to predict SPARC performance, showing remarkable agreement in the predicted machine performance. The POPCON analysis used to make the initial baseline estimates of SPARC performance in the scenarios described below is based on the following assumptions. The ITER $H_{98,y2}$ energy confinement time scaling relationship is used, as seen below:

$$\tau_E = 0.0562 H_{98,y2} I_p^{0.93} B_t^{0.15} n_{e,19}^{0.41} P_{loss}^{-0.69} R_0^{1.97} \kappa_a^{0.78} \epsilon^{0.58} M^{0.19}$$

The analyses in this manuscript are based on the $H_{98,y2}$ scaling relationship, which is a widely used multiplicative pre-factor (typically set to 1.0). The scaling equation takes into account various parameters such as plasma current (I_p), toroidal field on axis (B_t), line-averaged electron density ($n_{e,19}$), power loss through the separatrix via plasma transport (P_{loss}), plasma major radius (R_0), plasma elongation (κ_a), inverse aspect ratio (ϵ), and average ion mass (M). While other scaling relationships for energy confinement time in H-mode exist, the $H_{98,y2}$ scaling is the most commonly used in the analysis and comparisons presented in this paper, as shown in Figure 14.

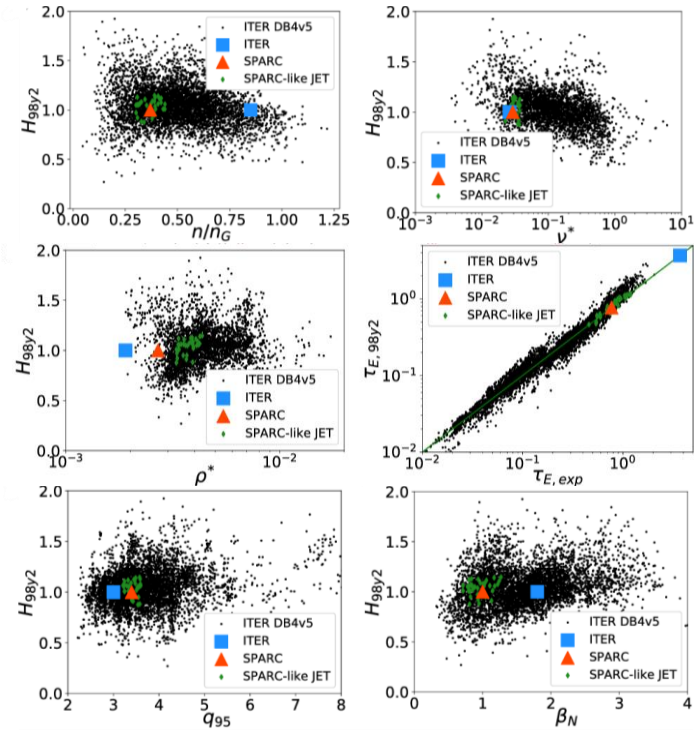

Figure 14: SPARC and ITER Operating Points Plotted Against Various Parameters from the ITER H-mode Database Db4v5 [19, 20]

Typically, in this analysis, $H_{98,y2}$ is assumed to be equal to 1. However, sensitivity studies have been conducted to evaluate the impact of lower confinement quality and different scalings for the energy confinement time in H-mode. It's worth noting that the performance estimate for the L-mode discharge utilizes the H_{89} energy confinement scaling law.

Both temperature and density profiles are assumed to exhibit peaking, which is quantified as v_x. Here, v_x represents the central value of quantity x divided by the volume average value. Density peaking is calculated using the empirical scaling [21, 22], while neglecting the neutral beam source from the original formula, as SPARC does not incorporate neutral beam injection.

$$v_{ne}^{Angioni} = 1.347 - 0.117 \ln\left(\frac{0.1 Z_{eff}(n_e) R_{geo}}{(T_e)^2}\right) - 4.03\left(\frac{4.02 \times 10^{-3}(p)}{B_T^2}\right)$$

In the given context, (n_e) represents the average density of the volume, measured in units of 10^{19} m^{-3}. Z_{eff} denotes the effective charge, R_{geo} represents the geometric radius of the plasma, measured in meters. T_e signifies the average temperature of the plasma volume, measured in kiloelectron volts (keV). Additionally, (p) denotes the average plasma pressure, measured in units of keV × 10^{19} m^{-3}, while B_T represents the toroidal magnetic field at the axis, measured in tesla (T).

To adopt a conservative approach, the electron density peaking, v_{ne}, is determined as $v_{ne}^{Angioni} - 0.1$ to align better with tokamaks utilizing inductively coupled radiofrequency heating and metal walls [23]. As for the ion density peaking, the scaling from the aforementioned equation is not directly applied due to possible contributions from impurity peaking. Central fuelling mechanisms such as pellets or beams are not considered in this analysis.

In the POPCON analysis, both electron and ion temperatures are assumed to be equal, with a peaking factor of $v_T = 2.5$, consistent with high-performance discharges observed in JET and ASDEX Upgrade experiments [21]. Notably, the empirically predicted temperature and density peaking factors for the SPARC V2 full-performance H-mode discharge, as shown in Table 5, align well with integrated modelling results based on physics-based transport and heating models [18].

For the plasma, Z_{eff} is assumed to be 1.5, and the main ion fraction (D-T) is set at 0.85, indicating that the main ion density is 85% of the electron density. These assumptions are consistent with relatively pure plasmas found in current metal-walled machines [24]. The analysis presented here assumes a 50-50 deuterium-tritium mix for the main ions.

Radiated power is calculated as the sum of bremsstrahlung and impurity radiation, employing the average ion model [25]. This calculation assumes a 6% helium concentration and a tungsten concentration of approximately 1.5 × 10^{-5}, consistent with results from ASDEX Upgrade [17] and JET ILW [27]. To maintain quasi-neutrality, a lumped Z = 8 impurity is included. In the parameter space relevant to high-performance SPARC operation, this calculation is found to be approximately equivalent to multiplying the calculated bremsstrahlung power by 2.25. It is important to note that impurity concentrations can vary significantly in existing machines, introducing considerable uncertainty when extrapolating to a new device. Boronization is planned as a potential technique to mitigate high impurity levels in SPARC.

Heating power in the system is composed of ohmic power, ICRH (Ion Cyclotron Resonance Heating), and fusion alphas. Ohmic power is determined using neoclassical resistivity, while the ICRH power required to achieve a specific temperature and density in the core plasma is obtained from the calculations. The ICRH power is limited by the total available radio-frequency power. Despite its relatively small magnitude

(around 1 MW), ohmic power is included in the fusion gain calculation as heating power.

The analysis evaluates access to and maintenance of H-mode using the Martin scaling [28], which is adjusted for the plasma isotope and accounts for the estimated core radiated power subtracted from the input power used for the threshold evaluation. The power considered in this scaling encompasses ohmic power, auxiliary heating power, and alpha power while subtracting the radiated power. Recent studies indicate that including the radiated power term is necessary for maintaining good H-mode confinement. Thus, we will take a conservative approach compared to the original scaling. Additionally, the analysis assumes that H-mode operation can only be sustained above this power threshold, disregarding the documented hysteresis in access power.

Approximate kinetic profiles are used to relate the separatrix shaping parameters in Table 4 to values at the 95% flux surface ($\kappa_{95} \approx \kappa_a = 1.75$ and $\delta_{95} \approx 0.45$). It should be noted that δ_{95} can vary significantly depending on the assumed or calculated kinetic profiles, making calculations based on this parameter inherently approximate. These values are utilized to determine the achievable plasma current and energy confinement time, as the $H_{98,y2}$ scaling employs the areal elongation $\kappa_a = \frac{S}{\pi a^2}$, where S represents the plasma cross-sectional area and a is the plasma minor radius. The achievable elongation for SPARC is estimated based on the performance of existing devices with a similar aspect ratio. The vertical stability of the plasma is subsequently confirmed through time-dependent TSC (time-dependent self-consistent) runs, incorporating realistic vertical stability coils and passive conductors [29].

The achievable plasma current for a given set of machine parameters is calculated assuming $q^* = 3.05$, where q^* is determined based on Uckan and the ITER Physics Group [30].

$$q^*_{Uckan} = \left(\frac{5a^2 B_0}{R_0 I_p}\right)\frac{1+\kappa_{95}^2(1+2\delta_{95}^2-1.2\delta_{95}^3)}{2}$$

All three operating scenarios described in this study (H-mode, L-mode, reduced-field H-mode) exhibit the magnetic equilibrium shown in Figure 12, with slight internal variations due to differences in parameters such as β. The equilibrium calculations were performed using the FreeGS Grad-Shafranov solver [31].

The full-performance H-mode scenario has received the majority of the analysis focus to date since it poses the highest demands on various engineering systems of SPARC. With a plasma current of 8.7 MA and $H_{98,y2} = 1$, SPARC achieves a fusion gain (Q) of approximately 11 and generates around 140 MW of fusion power. The operating space for this scenario is illustrated in a POPCON plot in Figure 13, and more detailed information about this operating point can be found in Table 5. To optimize the fusion gain, this scenario operates right at the L-H threshold, as calculated, although increasing the density and heating power would enable even higher fusion power (exceeding 250 MW) while maintaining Q≈10. However, caution must be exercised to avoid exceeding the allowable neutron heating of the toroidal field magnets. In terms of heating, most of the ICRH power is primarily absorbed by helium-3 minority ions, with some additional absorption at the second harmonic of tritium.

	8 T H-Mode	Full-Field H-Mode	Full-Field L-Mode	
B_0	8	12.2	12.2	T
I_p	5.7	8.7	8.7	MA
q^*_{Uckan}	3.05	3.05	3.05	
p^*	0.0036	0.0027	0.0031	
V_{eff}	0.13	0.16	0.04	
v^*	0.024	0.029	0.0073	
$H_{98y,2}/H_{89}$	1.0	1	1.0	
τ_E	0.65	0.77	0.44	s
P_{RF}	9.9	11.1	24.1	MW
P_{ohmic}	1.1	1.7	1.1	MW
Z_{eff}	1.5	1.5	1.5	
Main ion dilution	0.85	0.85	0.85	
(T_e)	5.6	7.3	9.7	keV
(T_i)	5.6	7.3	9.7	KeV
(n_e)	1.5	3.1	1.4	10^{20}m^{-3}
(n_i)	1.3	2.7	1.2	10^{20}m^{-3}
v_{Te}	2.5	2.5	2.5	
v_{ni}	1.36	1.33	1.51	
f_G	0.26	0.37	0.16	
β	0.010	0.012	0.007	
B	0.8	1.0	0.6	mTMA^{-1}
$P_{sep}B_0/R_0$	53	191	199	MW T m^{-1}
P_{fusion}	17	140	55	MW
Q	1.6	11.0	2.2	

Table 5: SPARC Performance Projection for D-T Plasmas

Even with significantly degraded confinement ($H_{98,y2} = 0.7$, two standard deviations below the mean of

the database), a full-field discharge is projected to achieve the primary mission of SPARC, which is Q>2. This margin allows for scenarios with highly dissipative divertor solutions that may result in core confinement degradation while still achieving the Q>2 mission. Additionally, SPARC is expected to meet the Q>2 mission when performance is evaluated using different $H_{98,y}$ scalings [32], the various energy confinement time scalings [33], and the proposed H20 scaling [34].

It should be noted that the dependence of Q on the volume-averaged density is sensitive to various details of the POPCON modelling, particularly the density peaking. Assuming a constant density peaking (independent of other parameters) generally leads to improved fusion gain with higher density. However, when density peaking is self-consistently calculated, moving to higher volume-averaged density tends to increase total power but decrease gain. Calculation of the density peaking, along with treatment of impurity radiation, contributes to the minor differences between the analyses. Nonetheless, the close agreement between analyses indicates the robustness of the design points to these assumptions. Even in the absence of density peaking (a completely flat density profile, which is unrealistic), the POPCON analysis suggests that SPARC should achieve Q≈4.

This discharge operates near the achievable elongation and slightly above q^*=3, which is often considered a reasonable limit for the safety factor [35]. Despite operating in this regime, SPARC remains well below known limits for β and density. The chosen density, which optimizes gain while staying within the allowable total fusion power, corresponds to a Greenwald fraction of only 0.37. The normalized β_N in this regime is approximately 1.0.

Regarding divertor heat flux, SPARC is designed to withstand the heat loads for the full 10 s flattop period with an attached, single-null plasma configuration (although double-null operation is also planned) using strike point sweeping. Empirical scalings for the heat flux width are utilized to determine the divertor heat loads. Although it may be possible for SPARC to achieve higher powers for shorter durations, the gain in these scenarios is expected to be lower, partially due to decreased density peaking at higher collisionalities. The L-H threshold power limits these scenarios from achieving higher gain, as indicated in Figure 13. However, it may be possible to operate at lower input power and achieve higher gain due to the hysteresis observed between entering and exiting H-mode [28].

In addition to the time-independent equilibrium shown in Figure 12, time-dependent scenarios have been developed using the time-dependent self-consistent approach. TSC simulations ensure that the desired flattop plasma can be achieved from plasma initiation to the end of the discharge, utilizing the SPARC V2 central solenoid and poloidal field coil set. TSC incorporates all central solenoid modules, poloidal field coils, vertical stability coils, and passive conducting structures such as the vacuum vessel and vertical stability plates. Lower current discharges impose fewer demands on the central solenoid and poloidal field coil set since the majority of the central solenoid flux is required to ramp the plasma to full current. Therefore, this first scenario sets most of the coil requirements for normal operation. Time-dependent transport simulations, including sawtooth and kinetic profile evolution, confirming that the plasma is well equilibrated within a few seconds into the current flattop.

To provide context, operational parameters of this SPARC discharge are compared to discharges in the ITER confinement database DB4v5 [23] and the inductive ITER reference discharge [19, 20]. Figure 14 presents this comparison in terms of $H_{98,y2}$, q_{95}, β_N, n/n_G, ν^*, ρ^*, and τ_E.

Where $\nu^* = 0.01 n_{e,20} \frac{q_{95} R Z_{eff} \left(\frac{R}{a}\right)^{\frac{3}{2}}}{T_{i,keV}^2}$,

And where $\rho^* = 4.57 \times 10^{-3} \frac{T_{i,keV} M^{-0.5}}{a B_t}$.

The database points used for comparison were carefully selected, including only standard aspect ratio tokamaks with the necessary data for each plot. In terms of stability limits, SPARC is positioned further from the limits than ITER in q_{95}, β_N, and n/n_G. It exhibits a very similar ν^* and requires no extrapolation for either ρ^* or τ_E, unlike ITER.

Figure 14 specifically highlights data from 25 JET discharges in the DB4v5 database that closely match the non-dimensional parameters of the SPARC operating point. $H_{98,y2}$, q_{95}, β_N, n/n_G, ν^*, and τ_E exhibit very close matches, although SPARC has a slightly smaller ρ^*. In essence, this suggests that no new plasma physics is required for the SPARC discharge (except for alpha physics), as non-dimensionally near-identical discharges have already been achieved on JET. While plasma physics is primarily governed by these non-dimensional parameters, it is important to note that fusion power depends on absolute density and temperature. Consequently, SPARC is expected to achieve significantly larger fusion power and gain compared to the devices included in this database, including JET.

In addition to the full-field H-mode discharge, the performance of SPARC in L-mode with full machine parameters has also been investigated. Operating in L-mode offers advantages by mitigating challenges associated with H-mode, such as edge localized modes and impurity accumulation. It also allows for the potential reduction of divertor heat flux by radiating a large fraction of the power from the core plasma while maintaining $H_{89} \approx 1$ [37]. Table 5 presents the projected performance of a full-field and full-current L-mode discharge in SPARC. The scenario achieves a fusion gain of $Q \approx 2.2$ with a fusion power of 55 MW, thereby fulfilling the primary mission of SPARC. The performance is mainly limited by the available radio-frequency power and the divertor's heat handling capacity.

Additionally, performance at reduced field and current has been considered. Particularly, performance at 2/3 of the toroidal field (8 T) is of interest, as the same resonant frequency for ion cyclotron range of frequencies (ICRH) that is used in the 12.2 T discharge is also resonant with a hydrogen minority at this reduced field. At 8 T, most of the ICRH power is absorbed by the hydrogen minority, with some additional power absorbed at the second harmonic of deuterium. Scenarios with fields on axis within approximately 1 T of either 8 T or 12 T are of primary interest to SPARC due to the favourable ICRH absorption in this range. This lower-field, lower-current scenario serves as an intermediate step towards full-field operation, demonstrating significant fusion power while remaining well below the majority of machine limits. As shown in table 5, operating at $B_0 = 8$ T and $q^* = 3.05$ corresponds to a 5.7 MA plasma and achieves a fusion gain of $Q \approx 1.6$ with 17 MW of fusion power. Although this falls short of the SPARC mission requirement of $Q > 2$, increasing the field to 8.6 T and the current to 6.2 MA does fulfill $Q = 2$. At 8.6 T, the ICRH will heat slightly off-axis on the low-field side. The lower volume-averaged temperature in this discharge also provides additional data for studying alpha physics and the interaction of alphas with MHD modes [36].

II.4. SPARC's Implementation Phase

Operating in H-mode is crucial for achieving peak performance in SPARC, and extensive efforts have been devoted to addressing H-mode accessibility and associated challenges, such as edge localized modes (ELMs) [38]. Although H-mode has been achieved in most modern diverted tokamaks, the physics of the L-H transition remains an area of active research, and the power required for the transition is still uncertain [28]. ELMs pose significant challenges in high-power-density devices due to transient loading on the divertor and other surfaces. Detailed discussions on these phenomena, as well as the ability to maintain high-quality H-mode confinement and the implications of reduced pedestal quality [38]. Studies have shown that SPARC can achieve its mission of $Q > 2$ even with a 50% degradation in pedestal pressure compared to the nominal prediction [38, 18].

One of the most challenging aspects of SPARC V2 and other burning plasma devices is heat exhaust due to the high-power density. Extensive research has focused on the performance of the divertor and its capability to handle the heat in a full-power deuterium-tritium (D-T) discharge [39]. The baseline scenario for SPARC V2 involves sweeping the attached divertor strike points, both inner and outer, to distribute the exhaust heat evenly across the divertor target. Early consideration of this operational scenario is crucial due to the strict requirements it imposes on power supplies and other systems. Given the uncertainty in achieving a perfect double-null configuration, the SPARC divertors are conservatively designed to operate in single-null configuration.

The empirical parallel heat flux width scaling ($\lambda_q \approx 0.2$ mm) with estimated peak unmitigated parallel heat fluxes of around 10 GW m^{-2} [1, 2] is an extrapolation for SPARC, and recent modelling studies predict wider heat flux widths in low-ρ^* plasmas. Therefore, data obtained from SPARC regarding divertor heat flux width scaling will provide important physics insights and help reconcile the differences between empirical scaling and modelling predictions. This conservative design approach does not exclude the exploration of detached divertor regimes, and SPARC will be able to test predictions regarding the impurity fractions required to induce detachment. Two-dimensional fluid modelling has been conducted to assess the possibility of detachment in SPARC. Divertor physics studies conducted on SPARC will inform the design and operation of the divertor in ARC, including the potential testing of an "advanced" X-point target divertor configuration.

SPARC's unique operating space, characterized by high field and current density, sets it apart from other high-performance tokamak regimes in terms of magnetohydrodynamics (MHD) [35]. While β-driven instabilities are expected to have a significantly reduced role compared to current devices, the large plasma current density raises concerns about disruptions and the resulting thermal and mechanical loads on the device.

Electromagnetic disruption loads have been evaluated using empirical scalings, and SPARC's mechanical structures are being designed to withstand these loads.

Plasma-facing components in the main chamber are also designed to withstand anticipated radiative heating during disruptions, accounting for appropriate peaking factors. Additionally, the generation and mitigation of runaway electrons in SPARC have been studied, building upon earlier work on SPARC V0 [40]. The possibility of incorporating a passive non-axisymmetric coil to reduce the likelihood of damage from runaway electron beams is also under consideration [41].

Given the high field and density in SPARC, Ion Cyclotron Resonant Heating (ICRH) is the preferred method for auxiliary heating. Extensive research has been conducted to assess the effectiveness of various ICRH operating scenarios and systems, considering either a hydrogen or helium-3 minority species as the primary target for power deposition. The heating of fast alpha particles is expected to be minimal, and the energy distribution of minority particles should not pose significant issues. The ICRH power source, transmission, and antenna systems have been planned, drawing on existing equipment, such as that from Alcator C-Mod.

One of the most intriguing aspects of SPARC physics is the presence of a large population of alpha particles. Careful attention is required to prevent alpha particles from damaging the device. Detailed neoclassical and ripple loss simulations suggest that first-wall heating resulting from alpha losses through these mechanisms will be modest. With a toroidal field ripple of 0.3% in SPARC V2, ripple-induced alpha losses are projected to be less than 1%. The interaction between alpha particles and high-frequency MHD modes is an area of interest, and initial investigations into the impact of high-field operation on the linear stability of Alfvén eigenmodes have been conducted [36]. This research suggests that the alpha physics regime in SPARC aligns closely with predictions for ITER, given the similar ion temperatures.

In addition to MHD interactions, SPARC will explore various other aspects of alpha and burning plasma physics, particularly if regimes with $Q \approx 11$ are attainable. These include alpha stabilization of turbulence, the interaction of alpha populations with sawtooth, and the self-consistent plasma profiles resulting from dominant alpha heating. The self-consistent distribution of alphas in space and energy within high-gain plasmas is a frontier research topic, and SPARC will build upon earlier work conducted on TFTR and JET.

III. Key Challenges and Considerations

After taking the in-depth analysis of both ITER and SPARC, we will now study some of the specific challenges when building a fusion reactor and what can be done to address them. One of the key challenges is achieving and maintaining plasma confinement and stability. The confinement of the hot plasma is crucial for achieving the necessary temperatures and densities for sustained fusion reactions. This requires controlling instabilities, such as plasma disruptions and edge localized modes (ELMs), which can lead to energy loss and damage to the plasma-facing components.

Another major consideration is the management of heat and particle exhaust. In a fusion reactor, the high-power density plasma generates immense heat that needs to be safely extracted and managed to prevent damage to the reactor components. The design of efficient divertor systems and advanced heat removal techniques are essential for handling the intense heat fluxes and particle fluxes associated with fusion reactions. Active research is focused on developing advanced divertor concepts, such as magnetic and material solutions, to effectively handle the heat and particle loads and maximize the reactor's performance.

Additionally, the production and sustainment of the plasma current pose significant challenges. A steady and reliable plasma current is required to maintain the magnetic confinement and initiate the fusion reactions. However, instabilities, such as disruptions and runaway electron generation, can disrupt the current flow and potentially damage the reactor. Efforts are being made to optimize the design and control of the magnetic field configuration, as well as to develop innovative techniques for current drive and plasma start-up, to ensure stable and continuous plasma operation.

Furthermore, the availability of suitable materials that can withstand the extreme conditions inside a fusion reactor is a crucial consideration. The high temperatures, intense radiation, and neutron fluxes impose strict requirements on the materials used in the reactor's structure and plasma-facing components. Ongoing research aims to develop advanced materials, such as tungsten alloys and ceramic composites, that can

withstand extreme conditions and maintain their structural integrity over the lifetime of the reactor.

Finally, it is essential to analyse the safety aspects of a fusion reactor compared to other energy sources. Safety considerations will play a vital role in determining the feasibility and viability of fusion becoming a viable source of energy production. Future and current fusion reactors, such as ITER and SPARC, face specific challenges that need to be addressed to ensure their safe operation.

III.1. Plasma Confinement and Magnetohydrodynamic Stability

Fusion power plants require reliable and robust plasma operating scenarios to avoid sudden disruptions that can potentially hinder fusion energy production. The economic viability of fusion power relies on maximizing the volume-averaged fusion power, which scales as $\beta^2 B_0^4$ [42]. Low-field approaches to fusion energy aim to operate near the beta limit. However, SPARC benefits from a strong toroidal field, enabling Q ≥ 2 operation even with lower values of normalized pressures (β_N = 1 and $\beta_p = (p)2\mu_0 B_p^2 = 0.79$, where B_p represents the poloidal field). This allows for more robust progress towards achieving fusion gain as it is less susceptible to MHD instabilities. The high plasma current (8.7 MA) raises the disruption density limit significantly above the density constraint imposed by the total fusion yield (≤140 MW). As a result, the normalized operating density is $n_G = n_e/(I_p/\pi a^2) = 0.37$, where n_e represents the electron density, I_p is the plasma current, and the plasma minor radius a. Despite the advantages of the high field, it does not significantly impact the plasma's vertical stability or current-driven resistive instabilities, which will be carefully considered in the SPARC design process.

While elongation increases the safety factor q_{95}, it also makes plasmas inherently prone to vertical instability, causing the plasma to move vertically towards the wall in what is known as a vertical displacement event (VDE). A VDE can be categorized as cold or hot, depending on whether the thermal energy is lost before or after the loss of vertical control. When the plasma comes into contact with the vessel wall, currents known as halo currents develop, leading to stresses on the conducting structures.

To guide the design of achievable plasma elongations, scaling laws and the ITER H-mode database have been investigated. However, the maximum elongation predicted by different scaling laws can vary, even for tokamaks with standard aspect ratios. Due to this ambiguity, the SPARC elongation design point is not significantly influenced by scaling laws but rather by utilizing the operating space defined by the ITER H-mode database. Figure 15 illustrates the ITER database in the context of the areal elongation $\kappa_a = S/\pi a^2$ and inverse aspect ratio $\iota = a/R$, where S represents the plasma cross-sectional area, and a and R are the plasma minor and major radii.

Theoretical studies on vertical stability provide metrics for passive stability and active stability that can be employed to assess reactors. We will examine the normalized vertical field decay index n relative to the critical index n_c across a database of stable and vertically unstable C-Mod discharges. This analysis helps validate the analytic theory and establish a relationship between a specific value of n/n_{crit} and expected disruptivity. The field decay index is defined as follows [43]:

$$n = \frac{R_0}{B_z}\frac{\partial B_z}{\partial R}$$

The critical index is determined by the following formula:

$$n_c = 2\left(\frac{\partial M_{vp}}{\partial z}\right)^2 \frac{R_0}{\mu_0 \Gamma L_v}$$

The mutual inductance between the plasma and the vacuum vessel is denoted as M_{vp}, the major radius of the magnetic axis is denoted R_0, and the vertical field at the axis is noted as B_z. The parameter Γ is calculated as $\frac{L_{ext}}{\mu_0 R_0} + \frac{l_i}{2} + \beta_p + \frac{1}{2}$, where L_{ext} and l_i represent the external and internal plasma inductances, β_p represents the plasma pressure normalized by the poloidal magnetic pressure, and L_v denotes the self-inductance of the vacuum vessel. The ratio n/n_{crit} plays a crucial role in determining the passive stability of the plasma, assuming a zero-resistivity wall. When $|n|/n_{crit}$ is less than 1, the plasma remains stable for time scales shorter than the resistive wall time and can be further stabilized for longer time scales using feedback control. On the other hand, when $|n|/n_{crit}$ exceeds 1, the vertical motion of the plasma approaches the Alfvén velocity.

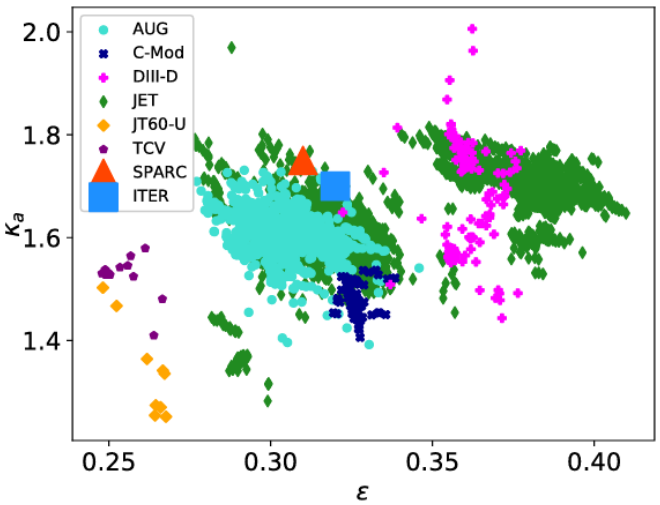

Figure 15: Areal Elongation and Inverse Aspect Ratio from Discharges in the ITER H-mode Database

To validate this approach, the n/n_{crit} formalism is applied to C-Mod discharges. Disruptive discharges that undergo vertical instability prior to the thermal quench are categorized and grouped based on the value of n/n_{crit} approximately 50 ms before the disruption. Subsequently, the total duration of C-Mod operation for each n/n_{crit} value is determined. By calculating the ratio of VDE counts to the corresponding duration in each bin, the disruptivity as a function of $|n|/n_{crit}$ is derived and visualized in Figure 2. The results reveal a transition from relatively low disruptivity (approximately 0.03 s^{-1}) to high disruptivity around $|n|/n_{crit} = 1.2$, aligning qualitatively with the theoretical expectations. However, the observed transition to instability occurs at a value approximately 20% higher than the theoretical prediction. This discrepancy may be attributed to calculation errors in n and n_{crit} or to the inherent assumption of a single-wall-mode in this formalism. Despite the 20% difference in the threshold, the n/n_{crit} parameter effectively distinguishes between low and high VDE disruptivity discharges. Notably, the disruptivity feature observed in the range of $0.2 \leq n/n_{crit} \leq 0.4$ is not yet fully understood due to the limited statistical significance of the data in those bins, and thus it is not considered significant. The evaluation of n/n_{crit} for the SPARC plasma, vacuum vessel, and vertical stability plate system is currently in progress, with the objective of achieving a value less than one.

In the design of SPARC V2, with an inverse aspect ratio of $\epsilon = 0.31$, a target elongation value of $\kappa_a = 1.75$ is selected. This specific region of phase space has been explored in ASDEX Upgrade and JET experiments, suggesting the attainability of such elongation values in high-performance discharges. However, it is acknowledged that the chosen high elongation values for the V2 design may reside in a marginally stable operational space. To enhance vertical control and enable operations at high elongation, a passive stability plate positioned between the vacuum vessel and the plasma is proposed. The complete plasma-conductor system, encompassing the vertical stability coils, stability plates, vacuum vessel, and poloidal field coils, has been subjected to simulation using the Tokamak Simulation Code (TSC), confirming stability [44].

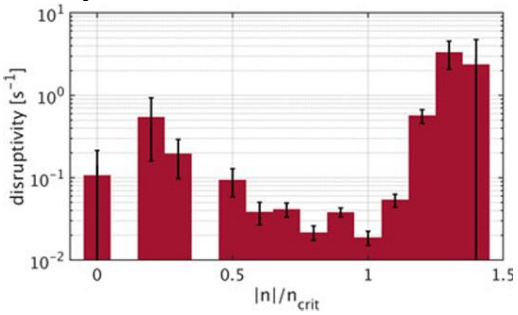

Figure 16: Histogram of the Disruptivity Attributable to Vdes In C-mod as a Function of the Stability Metric [44]

Figure 16 depicts the histogram illustrating the disruptivity attributable to VDEs in C-Mod as a function of the stability metric $|n|/n_{crit}$. Error bars are included to represent Poisson counting statistics. The bins at the extreme ends of the plot exhibit errors of 100%, causing the bars to exceed the lower limit of the logarithmic axis.

The ITPA scaling for $n = 1$ error field penetration in Ohmic plasmas predicts locked mode onset for overlap fields greater than $\delta_{pen,n1}B_T = 9.0$ G when operating in the full-field L-mode scenario. Note that this corresponds to the amplitude of the dominant external field which has a poloidal spectrum concentrated between $q_{99} \leq m \leq 2q_{99}$ at the normalized flux surface $\psi_N = 0.99$. It is unlikely that the intrinsic error field will have identically this poloidal spectrum, and thus a higher total $n = 1$ error field is likely acceptable. To prevent error field penetration, the component of the error field that overlaps with the dominant external field must be reduced well below 9.0 G. Further reductions will also be beneficial due to the reduced braking effect on the toroidal flow profile, with positive side effects for confinement and stability.

At this point, one can make a reasonable estimate of the maximum allowable intrinsic error field. Correction of the intrinsic error will require real-time algorithms that respond to the changing currents in the control coils contributing most strongly to the error. It seems prudent that one assumes these algorithms can predict the intrinsic error to no better than 50% at all times, giving a real-time prediction error of $\delta_{RT} = 0.5$.

This implies that 50% of the intrinsic error field cannot be larger than 9.0 G, or equivalently, the intrinsic error must be less than 18 G. Note that this 18 G corresponds to the amplitude of the dominant external field, but for the sake of conservatism, we will assume that this is the amplitude of the total $n = 1$ intrinsic error. Normalizing this intrinsic error by the toroidal field, we find 1.8×10^{-3} T/12.2 T = 1.5×10^{-4}.

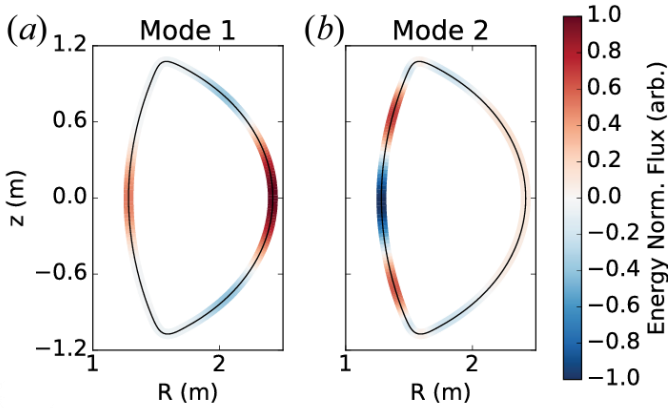

Figure 17 a & b: Dominant External Field Distributions as Predicted by GPEC for the Full-Field H-Mode Scenario [45]

The dominant external field is assessed in the full-field H-mode using the general perturbed equilibrium code (GPEC) [45, 46], and shown by the shaded boundary in Figure 17 (a). This mode structure concentrated about the outboard midplane is a result of the beta-driven ideal plasma response and is common to many devices, consistent with the success of the standard toroidal array of picture frame correction coils situated at the midplane. However, unlike present low-field machines, SPARC will access high plasma pressures at low β_N, reducing the ballooning nature of the ideal kink response that localizes it to the low-field side and thereby reduces the dominance of this single mode. The coupling of the second least-stable ideal kink response (Figure 17 (b)) to the core rational surfaces is only 50% smaller than the first, as shown in Figure 18, indicating that multi-mode error field correction might be important in SPARC. Also, the second mode is sensitive to inboard side errors, shown by the red and blue shaded regions in Figure 17(b), and thus attention will be paid to inboard side sources of errors in addition to the outboard errors. The plasma sensitivity to $n = 2$ field errors is also assessed (see Table 6), and $n = 2$ error field correction is under consideration.

	8 T H-Mode	Full-Field H-Mode	Full-Field L-Mode	Units
$\delta_{pen,n1}$	1.2	1.1	0.74	10^{-4}
$\delta_{pen,n2}$	7.3	9.1	3.2	10^{-4}

Table 6: The Toroidal Field Normalized Penetration Thresholds for n=1 and n=2 Fields During the Flattop Phase of the Three Main SPARC Operating Scenarios [48]

The target is a coil design that can apply the dominant external field with an amplitude of at least 18 G and that has the flexibility to continuously vary the toroidal phase of $n = 1$ and $n = 2$ fields. A midplane row of picture frame coils is planned to couple to the dominant field. Second-order effects arising from the non-resonant neoclassical toroidal viscosity torque can be addressed by adjusting the ratio of coil currents from the midplane and off-midplane correction coils [47]. A first design of the SPARC error field correction coil set expected to address this physics and consistent with engineering constraints is shown in Figure 18.

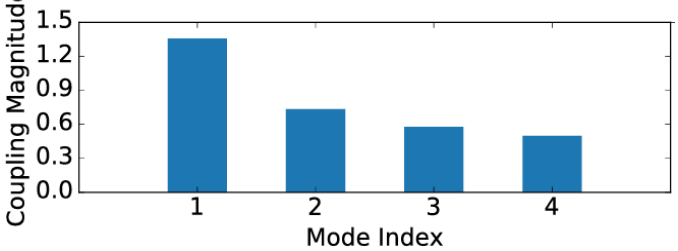

Figure 18: The Magnitude of the Coupling Between Fields and the Plasma [48]

The required correction currents in the proposed error field correction coil set are estimated by assessing the coupling to the dominant field. This is performed by a spectral analysis of the correction fields and by computing the inner product with the dominant field. The mid-plane coil array is found to have a coupling efficiency of $\mathcal{E}_c$ = 25 G kA^{-1}·turns. To produce a correcting field B_{cor} with an amplitude of 18 G using the midplane array only would require $I_c = B_{cor}/\mathcal{E}_c$ = 14 kA·turns. Providing a safety margin γ_{mgn} = 5, the midplane coil array will be designed to carry $I_{c,max}\gamma_{mgn}$ = 70 kA·turns. This design process to determine $I_{c,max}$ for a given coil design is summarized by the following equation:

$$I_{c,max} = \frac{\delta_{pen} B_T}{\delta_{RT} \mathcal{E}_c} \gamma_{mgn}$$

As mentioned above, the upper limit of the field (or current) generated by the error field correction coil set is determined by the plasma's sensitivity to the field, rather than the anticipated intrinsic error field of the machine. However, the sensitivity of the plasma to the intrinsic error, as predicted by the ITPA scaling, will be utilized to offer recommendations regarding the acceptable level of intrinsic error and, consequently, the manufacturing and assembly tolerances. To provide this engineering guidance, Monte Carlo simulations involving numerous combinations of coil tilts, shifts, and

shape errors will be conducted, following a similar approach employed for ITER [48].

III.2. Divertor Considerations

In order to ensure low erosion and minimize tritium co-deposition, future fusion reactors will need to utilize high-Z plasma facing components (PFCs). However, the current next step device, ITER, has adopted a material mix strategy to address different demands and operational flexibility. This approach involves using beryllium (Be) in the main chamber, tungsten (W) at the divertor baffles, and carbon (C) at the strikepoints. This choice is based on the favourable plasma-wall interaction properties of beryllium in the main plasma and the advantageous thermo-mechanical properties of carbon fiber composite (CFC). However, the unresolved issue of tritium co-deposition may necessitate the replacement of CFC components before tritium injection into ITER. Furthermore, in later phases of ITER operation and in future reactors, all PFCs will likely need to be transformed into high-Z components to gather operational data for reactor design. ASDEX Upgrade has implemented a W program to prepare for these decisions, gradually increasing the use of W PFCs in the main chamber since 1999. Although extrapolating these results to larger devices may pose challenges, they provide valuable benchmarks for modelling the implications of high-Z PFCs in a reactor.

The lack of a consistent set of atomic data for high-Z elements, including ionization-recombination coefficients and spectral emission data, presents a challenge. The cooling factor L_Z, which quantifies radiation loss, is commonly used to calculate total radiation from an element with density n_Z ($P_{rad,Z} = L_Z(T_e, n_e) \cdot n_Z \cdot n_e$). The average ion model (AIM) provides L_Z however lacks spectral distribution data. On the other hand, the distorted wave (DW) code HULLAC offers data for specific ion states but not in a comprehensive context with ionization and recombination data. To address this, an extension to the ADAS database has been developed, establishing an infrastructure with intermediate quality data for all ionization states. Collisional data were calculated using the plane-wave Born approximation (PWB) via the Cowan code.

While individual spectral lines require cautious interpretation, the PWB data are well-suited for analysing the radiated power of line arrays due to statistical cancellation of uncertainties. Excitation rate coefficients, A-values, and energy levels were calculated and used as inputs for a collisional-radiative model to derive level populations and spectral emissions for different plasma parameters. The abundance of each contributing ion state was determined using ionization and recombination data while considering transport effects. The VUV spectrum below 1.7 keV is dominated by a known quasi-continuum emitted by ionization states between W^{27+} and W^{35+}. Modelling successfully captured this part of the quasi-continuum but failed to reproduce emissions with wavelengths above 5.4 nm, even with additional ionization states included.

In a hot background plasma (>2 keV), spectral lines from W^{39+} to W^{45+} overlay the quasi-continuum emission and were accurately described by the model. In the soft x-ray (SXR) region, the majority of detectable tungsten emissions below 2 nm occur between 0.4 and 0.8 nm. Comparing measured and modelled spectra using the new excitation cross-sections from ADAS reveals small deviations in wavelength but overall satisfactory reproduction of the emission structure as seen in Figure 19.

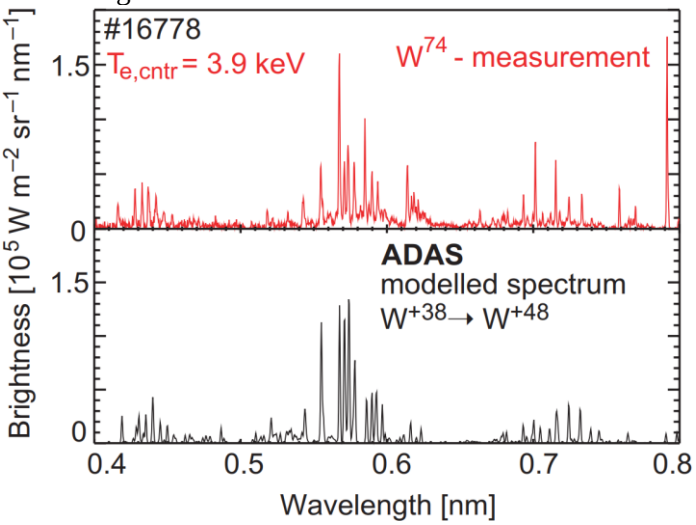

Figure 19: Comparison of Measured and Simulated SXR Spectra for Plasma Discharge with a Central Electron Temperature of 3.9 keV [27]

However, the strong E2 spectral line at 0.793 nm originating from Ni-like W is significantly underestimated, likely due to unconsidered inner shell ionization of W^{45+} (3d104s1) in the ADAS data. Modelling the SXR spectral features and interpreting total radiation with ADAS cooling factor data yield the same tungsten concentration, while using AIM data results in a concentration lower by a factor of 2.5. The cooling factors of tungsten from ADAS and AIM are compared, showing negligible differences above temperatures of 15 keV as continuum radiation becomes comparable to line radiation. This suggests that the maximum tolerable tungsten concentration in a reactor such as ITER is unaffected by this data revision.

Discharges conducted with upper single null (USN) configurations involve various modes (L- and H-modes) and high β_N plasmas. It was observed that discharges with low power neutral beam injection (NBI) heating exhibited increased tungsten concentrations (c_W). However, no significant difference in W content was found between USN and lower (C-based) divertor (LSN) discharges, even during a continuous transition from USN to LSN. Due to the limited pumping capacity in the upper divertor and the power load limitations of coated tiles, low-density improved H-modes could not be run in USN. Nevertheless, high-density discharges with high heating power were performed to investigate behaviour at high β_N and are depicted in Figure 20. These discharges achieved a β_N value of 2.8 with an H-factor ($H_{98,y2}$) of 0.95, along with a consistent low W concentration ($c_W \approx 2 \times 10^{-6}$) throughout the divertor.

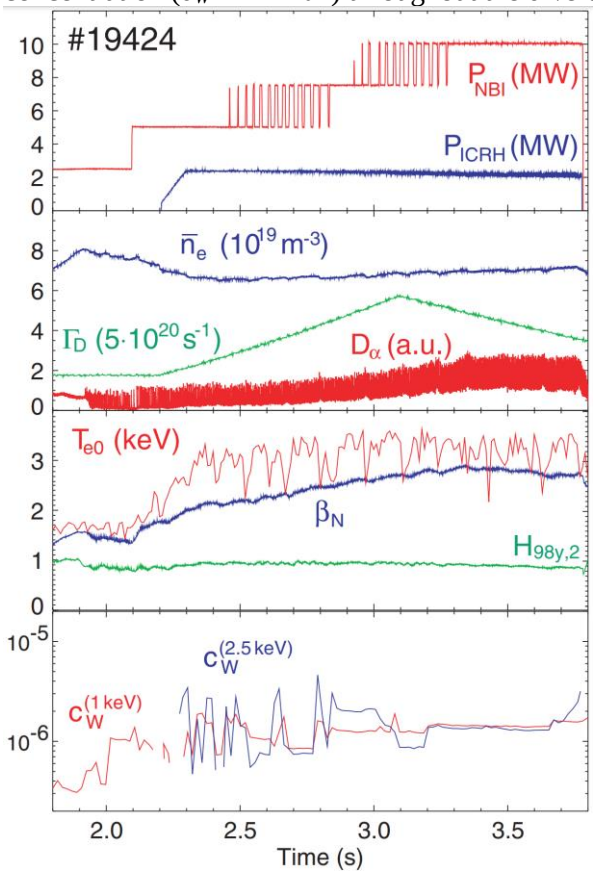

Figure 20: Time Traces for the USN Discharge #19424 With a Continuous Rise of the Auxiliary Heating Power [27]

Further optimization through a more sophisticated gas puffing program could potentially enhance performance. Thermographic views of the upper divertor, depicted in Figure 21, indicated power loads reaching up to 15 MW/m^2, and during ELMs, even higher values of 20-30 MW/m^2 were observed. Surface temperatures reached 700˚C at the discharge's end. In ordinary hydrogen discharges with a W divertor, no detectable W above the limit of about 2×10^{-7} was observed, likely due to reduced source from lower sputtering rates and reduced C contamination. The lower confinement and higher ELM frequency in hydrogen discharges may also contribute to lower W concentrations. These observations should be considered when extrapolating conclusions to deuterium or deuterium-tritium phases in future devices.

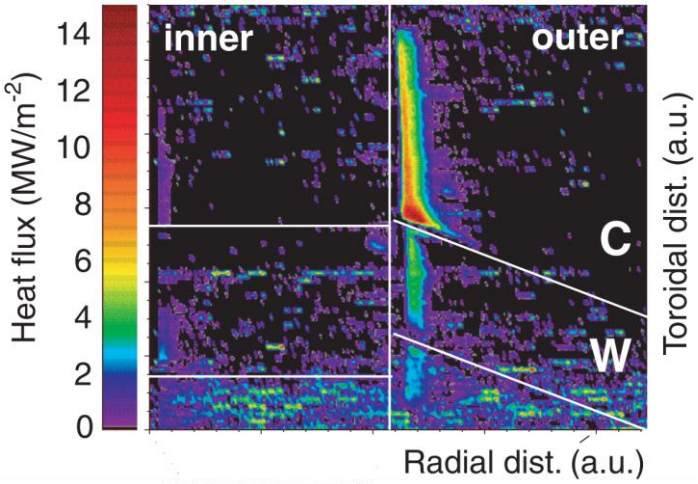

Figure 21: Heat Flux in the Upper Divertor In-between ELMs at 3.2 s [27]

SPARC will serve as a testbed for evaluating empirical scalings, computational models, and mitigation strategies relevant to fusion power plants. Empirical scalings based on heat flux width indicate a peak unmitigated parallel heat flux exceeding 6 GW/m² at the SPARC divertor target plates in the PRD scenario. The estimated surface heat flux profiles for the inner and outer divertor targets, assuming toroidally symmetric plates, suggest peak heat flux values of approximately 100 MW/m² for both divertors, with an incidence angle of around 0.95°. Tile shaping techniques are expected to increase the peak values by 50%.

Despite the desire for simplicity in design and construction and the limited overall lifetime, the divertor in SPARC is being engineered to withstand these heat loads without active cooling or remote handling, using well-established plasma-facing component materials. However, a significant challenge arises from the lack of maintenance in a radiation environment once nuclear operations begin, as both sustained D–D and D–T operations pose health and safety risks. Unlike many existing devices, SPARC, similar to ITER, does not plan to deploy a multi-campaign or upgrade strategy for its PFCs.

The decision to employ tungsten-based materials for the PFCs in SPARC was recently made after carefully weighing the trade-offs between low- and high-

Z material options and considering their associated risks. Although carbon-based PFC materials would be preferred in terms of improved manufacturability, reduced eddy current torques, and enhanced resistance to damage from thermal transients compared to tungsten, the tritium retention and high erosion rates of carbon-based materials do not align well with the goals of a pilot plant. The use of carbon-based materials would introduce a risk of not achieving SPARC's goals within the limited tritium inventory and specified timeline. Therefore, SPARC will incorporate a divertor made of tungsten-based tiles.

Due to the gap between current experiments and the divertor conditions anticipated in SPARC, it is uncertain whether a detached divertor compatible with high core confinement can be achieved. Consequently, SPARC is being designed under the conservative assumption of moderately dissipative divertor conditions, where approximately 50% of the power leaving the Last Closed Flux Surface (LCFS) is volumetrically removed before reaching the divertor. The power-sharing fractions assumed for divertor considerations adhere to the single-null equilibrium, with a 60/40 outer/inner split, even though SPARC aims to generate up-down symmetric equilibria.

In the PRD scenario of SPARC, the flexibility of the poloidal field and divertor coils will be utilized to perform a sweep of the strike point approximately once every second during the 10-second flattop phase. This sweeping motion is aimed at distributing the heat flux over a larger surface area of the divertor tiles, thereby keeping the surface temperatures within acceptable limits without the need for active cooling systems. As a result of the strike point sweep, localized spikes in surface temperature of the plasma-facing components will occur, but heat conduction into the bulk material will prevent tungsten from reaching its melting temperature. However, during certain events such as sweeping control failures, high-powered edge localized modes, and disruptions, it is inevitable to encounter short-term surface temperature excursions above the recrystallization limit. Monitoring and managing damage to the tungsten surface throughout the device's lifetime will be a significant challenge. The trajectory of the strike point sweep is being optimized to align with the capabilities of the power supply systems. Computational models such as UEDGE and SOLPS-ITER are being employed to predict divertor and edge conditions, as well as to identify impurity seeding and detachment requirements for high-power scenarios.

SPARC will serve as a platform for investigating potential solutions to achieve and control detached divertors under conditions relevant to fusion pilot plants. An advanced divertor mission, in addition to the primary mission of achieving $Q > 2$, drives the design of the device and the diagnostic requirements. The coil systems and divertor shapes are being designed to study different divertor configurations, including double-null, long-legged, and X-point target (XPT) divertors, which have been proposed for compact pilot plants due to their wide range of detachment power capabilities.

Although the XPT scenario in SPARC will not operate at full plasma current, it is expected to achieve $Q > 2$ and substantial fusion power, providing a unique platform for investigating advanced divertor scenarios. The effect of the secondary null location on power dissipation, as well as the sensitivity of detachment location and dissipation to external controls and transients, are being explored. Modelling work using UEDGE is underway to analyse the XPT configuration, and the requirements for controlling the X-point position are being evaluated. Many topics addressed by the advanced divertor mission align with those identified by the fusion community, with a focus on obtaining the minimum essential information needed to inform ARC while considering the limitations in measurement capabilities.

Projected unmitigated Type-I ELM frequencies in SPARC range from 3 to 15 Hz, with a peak parallel energy fluence of 11 to 32 MJ/m^2 at the divertor, similar to ITER projections. However, the surface heat flux loads in SPARC are expected to be smaller due to a lower angle of incidence. Estimated thermal loads during ELMs in the divertor result in heat flux factors ranging from 3.7 to 39 $MJ/m^2\ s^{-1/2}$ over significant portions of the divertor surface, allowing for exposure to one or a few ELMs. To expand the operational window of H-mode, increase safety margins, and ensure the survivability of the divertor PFCs, one should consider various extrinsic ELM mitigation techniques such as pellet injection, resonant magnetic perturbations, and plasma jogs. Additionally, small-ELM and intrinsically ELM-suppressed regimes, including I-mode and QH-mode, should be considered. Although these mitigation techniques often result in reduced pedestal pressure, given the ample margin the PRD scenario has for achieving $Q > 2$, it is expected that SPARC will successfully fulfill its primary mission even with the lower pedestal performance associated with reduced confinement.

In the PRD scenarios, unmitigated thermal quench disruptions are estimated to generate heat flux factors of up to 1 to 2 $GJ/m^2\ s^{-1/2}$ when considering

uncertainties in physics parameters. Such events would subject the material limits and cause top-surface melting of tungsten. Disruption mitigation measures will be implemented; however, the high-power density may still lead to heat flux factors of several tens of $MJ/m^2\ s^{-1/2}$ on the plasma-facing components in the main chamber, depending on the toroidal and poloidal peaking of the thermal quench. The effect of these high transient thermal loads on the bulk plasma-facing materials is being assessed through computational modelling and material testing.

III.3. Safety

The viability of fusion as a future energy source depends, in part, on its safety and environmental aspects. To ensure its feasibility, two fundamental objectives must be met:

1. Demonstrating that no accident would require the evacuation of the population.
2. Ensuring that waste does not become a burden for future generations.

The fusion reactor leverages its inherent advantages, such as the absence of the risk of a runaway reaction, and incorporates solutions through the implementation of low-activation materials in its design to address these objectives.

In terms of safety advantages, the primary fuels used in the fusion reactor, deuterium and lithium, are nonradioactive and nontoxic. The quantities of these elements required for daily energy generation are minimal, making their procurement, transport, and storage relatively straightforward.

The conditions for fusion reactions involve a low-density and pure plasma at high temperatures. The quantity of fuel present in the combustion chamber during the reaction is always very low. Any uncontrolled interference with the plasma environment leads to rapid cooling and automatic shutdown of the fusion reaction. The inherent processes in fusion reactions limit the possibility of uncontrolled power runaway, ensuring safety. Following the plasma shutdown, the residual energy is low, preventing major damage to the reactor's structures in the event of accidents.

The primary safety function to ensure in fusion reactors is confinement, as opposed to fission reactors that require control of the reaction and removal of residual power. The confinement strategy in fusion reactors is designed to minimize the diffusion of tritium, which exhibits high diffusion in most materials. The "multibarrier" approach, consisting of the vacuum vessel, the cryostat, and the reactor building itself, is adopted to minimize emissions in case of accidents. Detailed analyses have been conducted to assess energy inventories, potential accidents, and their expected consequences. These studies have shown that there are no accidental sequences that could compromise reactor integrity, and even in the event of a severe accident, evacuation of the surrounding population would not be necessary.

Regarding long-term radioactive waste, fusion reactors require minimal transport of radioactive materials, except for the initial tritium load during startup. After the fusion reactor's operational life, the materials surrounding the plasma and reactor structure become activated. By implementing low-activation materials, the induced radioactivity can be minimized. The quantity of materials considered for waste management varies depending on the reactor design, but after 100 years following the reactor's decommissioning, the majority of these materials can be classified as very low-activity waste or recycled within the nuclear industry. Comparatively, the average radioactivity of fusion reactor materials, even after 100 years of decay, is lower than that of the ash generated from an equivalent amount of coal used to produce the same energy, view Figure 22. Consequently, there is no need for deep storage of fusion waste, as the goal is to eliminate it within the generation that created it.

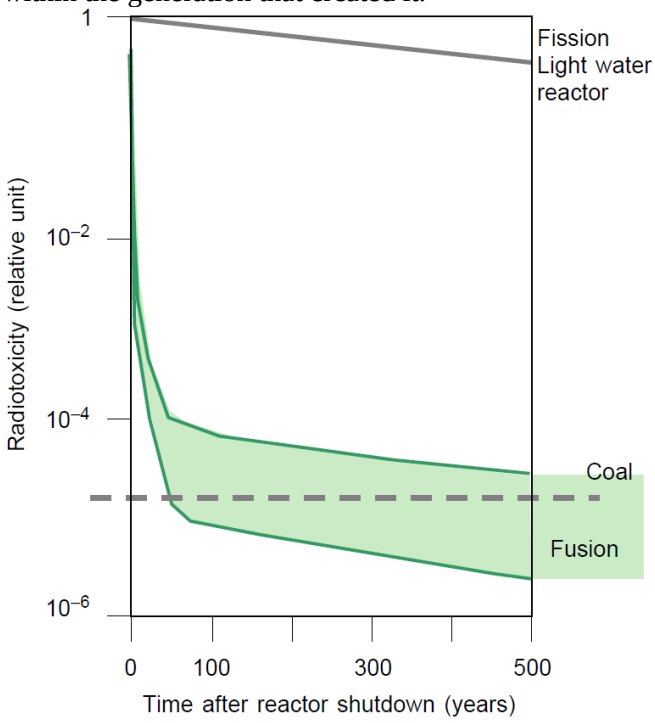

Figure 22: Radiotoxicity of Waste After Reactor Shutdown [49]

Hence, fusion reactors offer advantages in terms of safety and the absence of long-term radioactive waste. The use of nonradioactive fuels, low fuel quantities,

inherent safety features, and the implementation of low-activation materials contribute to the safe and sustainable operation of fusion reactors while minimizing their environmental impact.

IV. Economics, Cost, and Commercialization

Discussing kilowatt-hour production costs for an energy source that remains several decades away from commercialization might seem premature. However, conducting an economic analysis on a reactor such as ITER, holds significant value for a multitude of reasons.

Firstly, the primary objective of such an analysis is to illustrate the impact of various physical variables and technological production assumptions on costs. By examining these results, one can determine the relative orders of magnitude and directions of variation, which directly influence the development strategy. This information helps us make informed decisions about the feasibility and viability of fusion energy.

Secondly, it is essential to verify whether the proposed device aligns with market demand. The economic models used for this analysis are an extension of the models applied to the design, optimization, and cost calculations of current machines and projects. ITER shares many similarities with a typical fusion reactor, and its construction costs have been directly calculated by the involved industries in Europe, Japan, Russia, and the United States. Therefore, we have a solid evaluation basis to work with. While there are significant uncertainties regarding kilowatt-hour estimates, these uncertainties primarily revolve around reactor availability rather than the direct cost of its components.

When considering the direct costs, or internal costs, of energy production, they encompass expenses invoiced to consumers. These costs include plant construction, general operation, fuel purchases, and waste storage and dismantlement (specific to the nuclear industry). In the case of a fusion reactor such as ITER, fuel costs account for less than 1% of the total kilowatt-hour cost. Instead, the cost of energy generated by a fusion reactor is determined by the initial investment volume, augmented by the regular replacement costs of aging components (Figure 23).

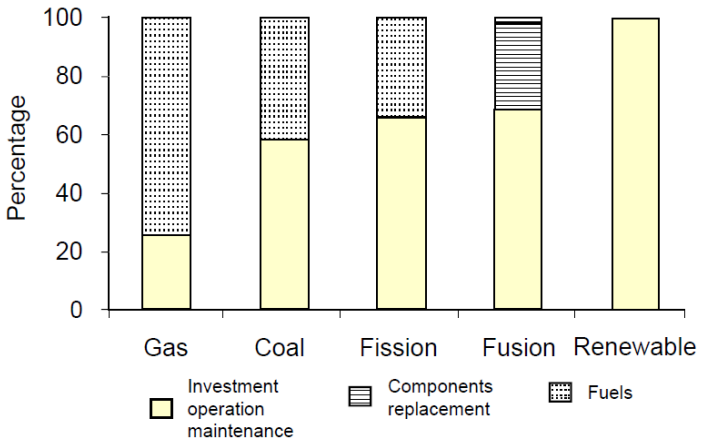

Figure 23: Breakdown of Direct Costs for Various Sources of Energy [49]

Comparing the standard volumes of fusion and fission reactors provides further insight. The combustion chamber of a fusion reactor typically has a volume on the order of 1000m³, whereas the reactor vessel volume of a fission reactor (1400MWe) is less than 300m³. Consequently, the investment requirements for fission reactors are high due to their larger size for the same sized combustion chamber. However, the absence of fuel costs in fusion partially compensates for this disadvantage when compared to conventional energy sources such as coal, gas, or fission. Nevertheless, current economic calculations estimate the cost of a fusion kilowatt-hour to be between $45 million and $90 million, with a probable value of approximately $65 million. This cost is roughly double that of conventional energy production (e.g., coal, gas, fission) and falls between the costs of offshore wind and photovoltaic production (assuming energy storage costs are not factored in for these latter sources).

It is important to note two key results. First, contrary to occasional claims, the production costs of fusion reactors would not automatically jeopardize the future of fusion energy. Second, fusion energy sources are characterized by high capital costs, emphasizing the need for careful economic evaluation.

Additionally, considering the concept of indirect costs, or external costs, is crucial for measuring the environmental impact of an energy production system. The European Union has developed a method called ExternE studies, which evaluates externalities associated with an energy production system. This method considers the identification of emissions attributable to the system, the transfer of pollutants in the environment, and the quantification of their environmental and health repercussions. It encompasses all stages of the reactor's lifecycle, including fuel extraction, plant construction, operation, accidents, and dismantlement. When applied

to fusion, this method demonstrates that the external costs of generating electrical energy through a fusion reactor are comparable to those of renewable sources and significantly lower than the costs associated with fossil-fuelled power as depicted in Figure 24.

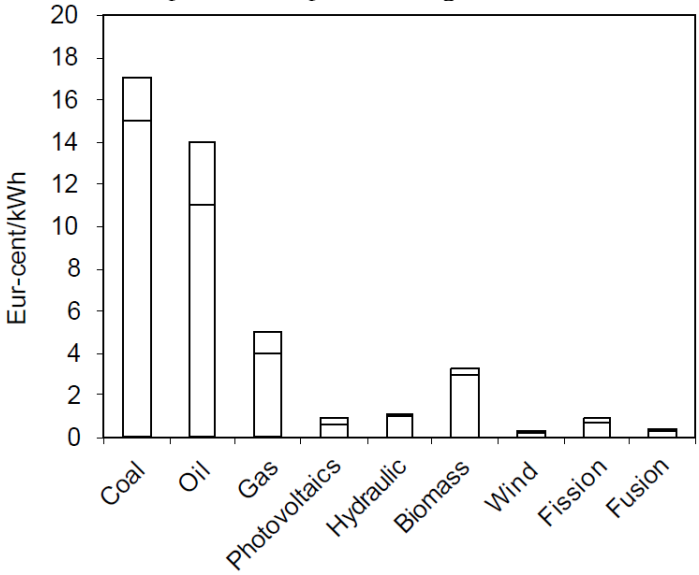

Figure 24: Comparison of Externalities of Several Energy Sectors [49]

In summary, conducting an economic analysis on ITER, the leading experimental fusion reactor, provides valuable insights into the impact of physical variables and technological assumptions on costs. It helps validate its compliance with market demand and ensures a solid evaluation basis due to the involvement of industries from Europe, Japan, Russia, and the United States. While fusion reactor production costs are characterized by a high capital investment, they would not automatically jeopardize the future of fusion energy. Moreover, considering external costs showcases the favourable environmental impact of fusion energy compared to fossil-fuelled power sources.

V. Conclusion

Fusion energy possesses a multitude of remarkable attributes. It stands as an almost limitless energy source, free from greenhouse gas emissions and environmental pollution, while providing undeniable safety benefits. Through thoughtful design, the radioactive waste generated by a fusion plant can be managed to avoid burdening future generations.

The pursuit of harnessing fusion energy is in alignment with its remarkable advantages. Although certain challenges remain, such as understanding plasma combustion physics, heat extraction, manufacturing sophisticated components like the blanket, and mitigating the effects of 14-MeV neutrons on materials, the scientific foundations are now robust enough to create a device that demonstrates the scientific and technological feasibility of fusion energy—this is the primary goal of the international ITER project.

The integration of fusion energy into the global energy landscape is envisioned to occur in the latter part of the 21st century, coinciding with the depletion of conventional resources and the climatic consequences of our current energy consumption. It is evident that this generation has a responsibility to prepare the knowledge base and expertise that will enable future decision-makers to thoughtfully consider all potential energy solutions. This serves as the objective of ongoing research in fusion technology.

Acknowledgment

The authors thank all who contributed to this article.

Declaration of Interests

The authors report no conflict of interest.

References

[1] T. Eich, A. W. Leonard, R. A. Pitts, W. Fundamenski, R. J. Goldston, T. K. Gray, A. Herrmann, A. Kirk, A. Kallenbach, O. Kardaun, and others, "Scaling of the tokamak near scrape-off layer heat flux width with plasma current, toroidal field, and collisionality," Plasma Phys. Control. Fusion, vol. 55, no. 12, 2013.

[2] D. Brunner, B. LaBombard, A. Q. Kuang, and J. L. Terry, "High-resolution heat flux width measurements at reactor-level magnetic fields and observation of a unified width scaling across confinement regimes in the Alcator C-Mod tokamak," Nucl. Fusion, vol. 58, no. 9, 2018.

[3] “ITER EDA AGREEMENT AND PROTOCOL 1,” ITER EDA Documentation Series No. 1, IAEA, Vienna, 1992.

[4] McGUIRE, K., ADLER, H., and ALLING, P. et al., Phys. of Plasma 2, pp 2176, 1995.

[5] THE JET TEAM PRESENTED BY GIBSON, A., “D-T Plasmas in JET: Behavior and Implications” to be published in Physics of Plasma, 1998.

[6] ISHIDA, S., FUJITA, T. and AKASAKA, H. et al., Phys. Rev. Letter. 79, pp 3917, 1997.

[7] IDE, S., FUJITA, T., and NAITO, O. et al., Plasma Physics and Controlled Fusion 38, pp 1645, 1996.

[8] “ITER COUNCIL PROCEEDINGS: 1992,” ITER EDA Documentation Series No. 3, pp 53, IAEA, Vienna, 1994.

[9] “ITER COUNCIL PROCEEDINGS: 1998” to be published in ITER EDA Documentation Series, IAEA, Vienna 1998.

[10] CAMPBELL, D. J. et al., “ITER Physics Basis and Physics Rules,” IAEA-F1-CN69/ITER/1.

[11] IAEA. "Overview of the Design and R&D Activities for the ITER Vacuum Vessel and In-Vessel Components." IAEA, IAEA-TECDOC-1399, International Atomic Energy Agency, Vienna, Austria, 2004.

[12] CHOPPIN, GREGORY R. “Fusion Reaction - an Overview | ScienceDirect Topics.” w*ww.sciencedirect.com*, 2017, www.sciencedirect.com/topics/engineering/fusion-reaction.

[13] G, A. “ITER Tokamak Fusion Reactor.” *Fusion for Energy*, 2022, fusionforenergy.europa.eu/the-device/. Accessed 12 Apr. 2023.

[14] PERKINS, F., et al., Plasma Physics and Controlled Fusion, (Proc. 24th Eur. Conf. Berchtesgarten, 1997) 21A 1017 (1997).

[15] G. Federici et al., "DEMO design activity in Europe: Progress and updates," Fusion Engineering and Design, vol. 136, Part A, pp. 729-741, 2018. DOI: 10.1016/j.fusengdes.2018.04.001.

[16] Nave, R. “Nuclear Fusion.” *Gsu.edu*, 2019, hyperphysics.phy-astr.gsu.edu/hbase/NucEne/fusion.html. Accessed 12 Apr. 2023.

[17] R. Neu, R. Dux, A. Kallenbach, T. Pütterich, M. Balden, J.C. Fuchs, A. Herrmann, C.F. Maggi, M.O. Mullane, R. Pugno, et al., "Tungsten: an option for divertor and main chamber plasma facing components in future fusion devices," Nucl. Fusion, vol. 45, no. 3, 2005.

[18] P. Rodriguez-Fernandez, N. T. Howard, M. J. Greenwald, A. J. Creely, J. W. Hughes, J. C. Wright, C. Holland, Y. Lin, F. Sciortino, and the SPARC Team, "Predictions of core plasma performance for the SPARC tokamak," J. Plasma Phys., vol. 86, 2020, doi: 10.1017/S0022377820001075.

[19] V. Mukhovatov, M. Shimada, K. Lackner, D. J. Campbell, N. A. Uckan, J. C. Wesley, T. C. Hender, B. Lipschultz, A. Loarte, R. D. Stambaugh et al., "Chapter 9: ITER contributions for DEMO plasma development," Nucl. Fusion, vol. 47, no. 6, pp. S404-S413, 2007.

[20] M. Shimada, D. J. Campbell, V. Mukhovatov, M. Fujiwara, N. Kirneva, K. Lackner, M. Nagami, V. D. Pustovitov, N. Uckan, J. Wesley, "Chapter 1: overview and summary," Nucl. Fusion, vol. 47, no. 6, pp. S1-S17, 2007.

[21] C. Angioni, H. Weisen, O. J. W. F. Karduan, M. Maslov, A. Zabolotsky, C. Fuchs, L. Garzotti, C. Giroud, B. Kurzan, P. Mantica, et al., "Scaling of density peaking in H-mode plasmas based on a combined database of AUG and JET observations," Nucl. Fusion, vol. 47, no. 9, pp. 1326-1335, 2007.

[22] C. Angioni, E. Fable, M. Greenwald, M. Maslov, A. G. Peeters, H. Takenaga, and H. Weisen, "Particle transport in tokamak plasmas, theory and experiment," *Plasma Phys. Control. Fusion*, vol. 51, no. 12, p. 124017, 2009.

[23] M. Greenwald, C. Angioni, J. W. Hughes, J. Terry, and H. Weisen, "Density profile peaking in low collisionality H-modes: comparison of Alcator C-Mod data to ASDEX Upgrade/JET scalings," Nucl. Fusion, vol. 47, no. 9, pp. L26-L29, 2007.

[24] F. Romanelli and JET EFDA Contributors, "Overview of the JET results with the ITER-like wall," Nucl. Fusion, vol. 53, no. 10, p. 104002, 2013.

[25] R. V. Jensen, D. E. Post, W. H. Grasberger, C. B. Tarter, and W. A. Løkke, "Calculations of impurity radiation and its effects on tokamak experiments," *Nucl. Fusion*, vol. 17, no. 6, pp. 1187-1196, 1977.

[26] Thomsen, K. & The H-Mode Database Working Group. (2002). "The international global H-mode confinement database: storage and distribution." Fusion Engng Des. 60 (3), 347–352

[27] R. L. Neu, S. Brezinsek, M. Beurskens, V. Bobkov, P. de Vries, C. Giroud, E. Joffrin, A. Kallenbach, G. F. Matthews, M. Mayoral, et al., "Experiences with tungsten plasma facing components in ASDEX Upgrade and JET," IEEE Trans. Plasma Sci., vol. 42, no. 3, pp. 552-562, 2014.

[28] Y. R. Martin, T. Takizuka, and the ITPA CDBM H-Mode Threshold Data Group, "Power requirement for accessing the H-mode in ITER," J. Phys.: Conf. Ser., vol. 123, p. 012033, 2008

[29] S. C. Jardin, N. Pomphrey, and J. DeLucia, "Dynamic modeling of transport and positional control of tokamaks," *J. Comput. Phys.*, vol. 66, pp. 481-507, 1986.

[30] N. A. Uckan and the ITER Physics Group, "ITER physics design guidelines: 1989," IAEA.

[31] FreeGS: A Grad-Shafranov Solver [Software]. Available: https://github.com/bendudson/freegs

[32] ITER Physics Expert Group on Confinement and Transport, ITER Physics Expert Group on Confinement Modeling and Database, ITER Physics Basis Editors. (1999). "Chapter 2: Plasma Confinement and Transport." Nucl. Fusion 39 (12), 2175–2249.

[33] Verdoolaege, G., Kaye, S. M., Angioni, C., Kardaun, O., Maslov, M., Romanelli, M., Ryter, F., & Thomsen, K. (2018). "First analysis of the updated ITPA global H-mode confinement database." In Proceedings of the 27th IAEA Fusion Energy Conference, p. 8. International Atomic Energy Agency.

[34] Verdoolaege, G., Kaye, S. M., Angioni, C., Kardaun, O. J. W. F., Maslov, M., Romanelli, M., Ryter, F., & Thomsen, K. (2020). "The updated ITPA global H-mode confinement database: description and analysis." In ITPA Transport & Confinement Topical Group Meeting.

[35] Sweeney, R., Creely, A. J., Doody, J., Fülöp, T., Garnier, D. T., Granetz, R., Greenwald, M., Hesslow, L., Irby, J., Izzo, V. A., et al. (2020). "MHD stability and disruptions in the SPARC tokamak." J. Plasma Phys. 86.

[36] Tolman, E. A., Loureiro, N. F., Rodrigues, P., Hughes, J. W., & Marmar, E. S. (2019). "Dependence of alpha-particle-driven Alfvén eigenmode linear stability on device magnetic field strength and consequences for next-generation tokamaks." Nucl. Fusion, 59(4), 046020.

[37] GREENWALD, M., BOIVIN, R. L., BOMBARDA, F., BONOLI, P. T., FIORE, C. L., GARNIER, D., GOETZ, J. A., GOLOVATO, S. N., GRAF, M. A., GRANETZ, R. S., et al. 1997 H-mode confinement in Alcator C-Mod. Nucl. Fusion 37 (6), 793–807.

[38] J. W. Hughes, N. T. Howard, P. Rodriguez-Fernandez, A. Q. Kuang, E. A. Tolman, A. J. Creely, and P. B. Snyder,

"High confinement access and edge pedestal structure in the SPARC tokamak," J. Plasma Phys., vol. 86, no. 6, 2020.
[39] A. Q. Kuang, S. Ballinger, D. Brunner, J. Canik, A. J. Creely, T. Gray, M. Greenwald, J. W. Hughes, J. Irby, B. LaBombard, and others, "Prediction and mitigation of divertor heat fluxes in SPARC," J. Plasma Phys., vol. 86, no. 6, 2020.
[40] T. Fülöp, P. Helander, O. Vallhagen, O. Embreus, L. Hesslow, P. Svensson, A. J. Creely, N. T. Howard, and P. Rodriguez-Fernandez, "Effect of plasma elongation on current dynamics during tokamak disruptions," J. Plasma Phys., vol. 86, no. 1, 2020.
[41] A. H. Boozer, "Two beneficial non-axisymmetric perturbations to tokamaks," Plasma Phys. Control. Fusion, vol. 53, no. 8, 2011.
[42] J. A. Wesson, "Tokamaks, 3rd edn.," Oxford University Press, 2005
[43] E. A. Lazarus, J. B. Lister, and G. H. Neilson, "Control of the vertical instability in advanced tokamak," Nucl. Fusion, vol. 30, no. 1, pp. 111-141, 1990.
[44] J. C. Jardin, N. Pomphrey, and J. Delucia, "Dynamic modeling of transport and positional control of tokamaks," J. Comput. Phys., vol. 66, no. 2, pp. 481-507, Nov. 1986.
[45] J. K. Park, A. H. Boozer, J. E. Menard, A. M. Garofalo, M. J. Schaffer, R. J. Hawryluk, S. M. Kaye, S. P. Gerhardt, and S. A. Sabbagh, "Importance of plasma response to nonaxisymmetric perturbations in tokamaks," Phys. Plasmas, vol. 16, no. 5, 2009.
[46] J. K. Park and N. C. Logan, "Self-consistent perturbed equilibrium with neoclassical toroidal torque in tokamaks," Phys. Plasmas, vol. 24, no. 3, 2017.
[47] Y. Gribov, V. Amoskov, E. Lamzin, N. Maximenkova, J. E. Menard, J. K. Park, V. Belyakov, J. Knaster, and S. Sytchevsky, "Error fields expected in ITER and their correction," in Proceedings of 24th International Conference on Fusion Energy, San Diego, CA, 2012, pp. 154_ITRP529.
[48] N. C. Logan, L. Cui, H. Wang, Y. Sun, S. Gu, G. Li, R. Nazikian, and C. Paz-Soldan, "Magnetic polarization measurements of the multi-modal plasma response to 3D fields in the EAST tokamak," Nucl. Fusion, vol. 58, no. 7, p. 076016, 2018.
[49] P. Magaud, G. Marbach, and I. J. Cook, "Nuclear Fusion Reactors," 2004.